

FAPE-IR: Frequency-Aware Planning and Execution Framework for All-in-One Image Restoration

Jingren Liu^{1*}, Shuning Xu^{2*}, Qirui Yang^{1*}, Yun Wang³, Xiangyu Chen^{4†}, Zhong Ji^{1†}

¹Tianjin University

²University of Macau

³City University of Hong Kong

⁴Institute of Artificial Intelligence (TeleAI), China Telecom

Abstract

All-in-One Image Restoration (AIO-IR) aims to develop a unified model that can handle multiple degradations under complex conditions. However, existing methods often rely on task-specific designs or latent routing strategies, making it hard to adapt to real-world scenarios with various degradations. We propose FAPE-IR, a Frequency-Aware Planning and Execution framework for image restoration. It uses a frozen Multimodal Large Language Model (MLLM) as a planner to analyze degraded images and generate concise, frequency-aware restoration plans. These plans guide a LoRA-based Mixture-of-Experts (LoRA-MoE) module within a diffusion-based executor, which dynamically selects high- or low-frequency experts, complemented by frequency features of the input image. To further improve restoration quality and reduce artifacts, we introduce adversarial training and a frequency regularization loss. By coupling semantic planning with frequency-based restoration, FAPE-IR offers a unified and interpretable solution for all-in-one image restoration. Extensive experiments show that FAPE-IR achieves state-of-the-art performance across seven restoration tasks and exhibits strong zero-shot generalization under mixed degradations.

1. Introduction

Image restoration seeks to recover clean images from degradations such as rain, snow, fog, blur, low-light, and noise, and is fundamental to safety- and quality-critical applications in medical imaging [7, 84], consumer photography [101], and autonomous driving [25, 42, 87]. Traditional pipelines typically employ specialized architectures or optimization strategies for each type of degradation [28, 63, 107, 112]. Although recent single-degradation models report strong results on curated benchmarks [20,

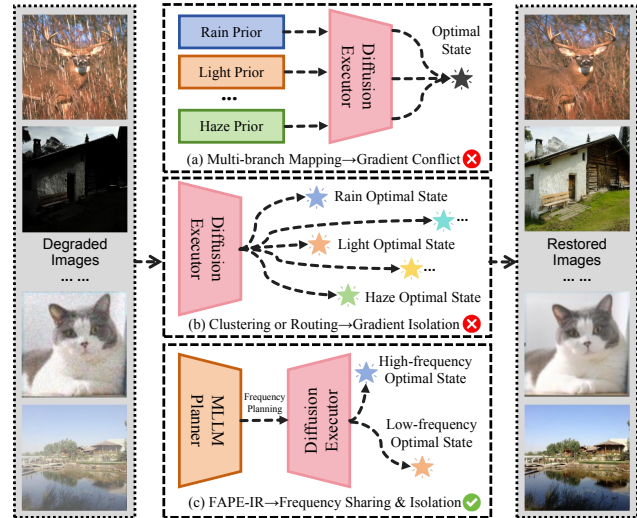


Figure 1. Comparison of AIO-IR methods: (a) multi-branch mappings with task-level priors; (b) task-specific routing/clustering; (c) our FAPE-IR, unifying understanding and restoration.

[31, 85, 100, 115], real-world images rarely present a single known corruption; degradations are often unknown, co-occurring, and subject to distribution shift, which undermines stability and controllability. This gap motivates All-in-One Image Restoration (AIO-IR), which aims to handle multiple degradations within a single model [8, 10, 11, 49, 59, 68, 78, 106]. Yet most current efforts still assume task separability [1, 49] or tether restoration to reconstruction pipelines driven by task-level priors [86, 96], preventing models from autonomously perceiving and disentangling degradation attributes. As a result, model generalization to real-world scenarios remains inadequate.

Within current AIO-IR methods, a prevailing strategy is to employ multi-branch mappings (see Figure 1-(a)), injecting task-level conditions via explicit priors (e.g., prompts, embeddings, or specialized encoders) and learning the restoration paths accordingly [8, 39, 50, 51, 57, 114]. This design is prone to severe cross-task interference. In a uni-

*Equal contribution.

†Corresponding author.

fied model with shared parameters, gradients from different degradations conflict, making it difficult to reach task-specific optima simultaneously. Moreover, both training and inference depend on prior labels or textual inputs, incurring substantial annotation and prompt-engineering costs. A complementary strategy clusters features or employs specialized routing mechanisms within the model (see Figure 1-(b)) [13, 15, 78, 90, 109, 113]. Because tasks are strongly separated in latent space, their learning processes become nearly independent, which hampers the discovery of shared structures and compositionality across degradations. Consequently, robustness to compound degradations is limited, and generalization suffers. More critically, both lines lack semantic understanding and rely on opaque degradation pipelines, hindering content-aware adaptation and interpretability. These limitations call for a unified, semantics-aware AIO-IR framework in which degradation understanding and restoration are coupled, and task knowledge is both disentangled and shared in an adaptive way.

To instantiate such a framework, we adopt diffusion-based image restoration, which has recently become a popular choice for AIO-IR due to its strong generative priors [8, 13, 15, 57, 90, 113, 114]. This formulation naturally models diverse degradations, yet prior work typically treats diffusion as a task-conditioned generator driven by labels or hand-crafted priors, leaving degradation modeling opaque and under-exploiting cross-degradation interactions. We instead regard diffusion as the execution engine in a unified multimodal understanding-generation paradigm. In this paradigm, degradations are first parsed and organized, and then restored. Inspired by recent unified models [9, 17, 40, 95, 99, 102], we instantiate FAPE-IR, a multimodal large language model (MLLM) + diffusion framework for low-level vision (see Figure 1-(c)). An MLLM explicitly parses image content and degradation semantics and outputs understanding and planning tokens that condition a diffusion executor to perform content-adaptive restoration in the frequency domain, grouping tasks into high- and low-frequency regimes, thereby encouraging sharing within same-frequency tasks and isolating conflicting ones.

Concretely, FAPE-IR couples a multimodal planner with a diffusion-based executor to mitigate cross-task gradient conflict and isolation from a frequency perspective. In the planning stage, we employ a label-free procedure to extract as many degradation-related low-level features as possible, and introduce several well-designed instructions that constrain the model to output: the degradation types present in the image, the primary frequency bands requiring restoration, the underlying causes, and the proposed restoration pipeline. This design yields effective, per-image understanding that more accurately guides the restoration process. In the execution stage, tokens produced by the planner, augmented with high-/low-frequency visual features from

SigLIP-v2 [79] and a VAE [30], guide the restoration of the entire image. Furthermore, we propose a Frequency-Aware LoRA-MoE architecture, where text tokens from the planner and the high-/low-frequency signals extracted from intermediate executor’s features drive the MoE gating to select among high-/low-frequency experts dynamically and interpretably. For the overall training recipe, we provide theoretical and empirical evidence that adversarial training on diffusion-pretrained weights can yield higher fidelity and fewer artifacts than other fine-tuning methods under our setting. Building on this, we further introduce an energy-based frequency regularization loss so that each frequency expert is optimized in its most suitable band.

Our main contributions are summarized as follows: (i) We introduce FAPE-IR, a unified understanding-generation AIO-IR framework that couples a multimodal planner with a diffusion-based executor, enabling semantics-driven, content-adaptive restoration across diverse degradations. (ii) We develop a frequency-aware modeling strategy that dynamically routes information between high- and low-frequency experts, mitigating cross-task interference while promoting shared representations among related tasks. (iii) We conduct comprehensive experiments on a wide range of single-degradation and mixed-degradation benchmarks, demonstrating that FAPE-IR achieves state-of-the-art or competitive performance and exhibits strong zero-shot generalization to unseen compound degradations.

2. Related Works

2.1. Diffusion-based AIO-IR

In recent years, diffusion-based AIO-IR methods have advanced rapidly. Existing approaches fall into two families: (i) multi-branch mappings and (ii) clustering or routing. The former relies on injecting task-level priors into a shared backbone via task encoders or textual/latent prompts. PromptIR [58], Prompt-in-Prompt [39], and InstructIR [14] unify degradations through prompts or instructions. ProRes [51] and DA-CLIP [50] supply content/degradation embeddings via visual prompts or CLIP [61] controllers and fuse them with cross-attention. UniRestore [8] injects task cues into diffusion, whereas UniRes [114] composes task specialists at sampling time. The latter adapts internal representations by clustering features or routing to experts. AdaIR [15] and DFPIR [78] mine frequency cues and reshape separable, degradation-aware features. AMIR-Net [110] performs label-free, layer-wise clustering with domain alignment. Within diffusion, DiffUIR [113] disentangles shared/private factors for selective routing. MoCE-IR [109] and M2Restore [90] use complexity-aware MoE to activate only necessary experts. Overall, these strategies improve efficiency but lack sample-level planning, relying on fixed task-level designs and ignoring whether tasks

should share or isolate knowledge. This leads to under-shared representations, misrouting, and artifacts under unknown or composite degradations, limiting open-world robustness. To address this, we propose FAPE-IR, a unified understanding-generation framework.

2.2. Unified Models

A central goal of multimodal AI is to develop general-purpose foundation models that can jointly understand and generate diverse modalities within a single framework. Recent unified models largely follow three paradigms. Multimodal autoregression methods, such as Chameleon [77], Emu3 [89], and UGen [76], tokenize images into a shared discrete space and train a single decoder-only Transformer, but this tokenization degrades fine details and incurs long generation latency, limiting their suitability for precise low-level restoration. Multimodal diffusion approaches instead unify modalities at the denoising stage: MMaDA [102] employs a modality-agnostic diffusion backbone with unified post-training; LaViDa [36] uses elastic masked diffusion for understanding, editing, and generation; Dimple [108] couples an autoregression warm-up with discrete diffusion and parallel confident decoding; and UniDisc [75] casts joint text–image modeling as discrete diffusion in a shared token space. However, this paradigm remains nascent, with unresolved issues in consistency and inference efficiency. A third line, MLLM+Diffusion frameworks, decouple high-level multimodal understanding from generation: UniWorld-V1 [40] conditions diffusion on high-resolution semantic features from MLLMs and contrastive encoders; BAGEL [17] integrates decoder-only MLLMs with diffusion heads in an “integrated Transformer” for both understanding and image generation; Janus [95] decouples visual encoding for understanding versus generation under a unified backbone; and BLIP3-o [9] uses CLIP-based semantic spaces with diffusion transformers and staged pre-training to balance image understanding and generation. Yet these conditioning interfaces are primarily designed for high-level semantic editing or creation, rather than pixel-accurate, artifact-free restoration. Our FAPE-IR framework follows the MLLM+Diffusion paradigm but is specialized for low-level image restoration, where fine-grained controllability and artifact suppression are central.

3. Methodology

As shown in Figure 2, FAPE-IR adopts a planning and execution paradigm that decomposes image restoration into a frequency-aware planner and a band-specialized restoration executor. In the remainder of this section, we first describe the frequency-aware planner, including the construction of a label-free low-level feature pool, instructions and planning, and the encoding of frequency-aligned understanding tokens (Section 3.1). We then present the pro-

posed Frequency-Aware LoRA-MoE architecture in executor (Section 3.2). Finally, we introduce the adversarial training strategy and the overall loss formulation, which couples frequency-aware routing with perceptual and adversarial supervision (Section 3.3).

3.1. Frequency-aware Planner

Label-free Low-level Feature Pool. Given a degraded input image c , we first construct a label-free low-level feature pool that characterizes its degradation pattern from a frequency perspective. Specifically, we compute a vector of simple image statistics P_{hints} directly from pixel values, without relying on degradation labels or auxiliary metadata. Each component of P_{hints} corresponds to one of seven representative degradation types: for **rain**, the strength of oriented streaks; for **snow**, the density of small bright blobs; for **noise**, luminance and chroma variations in flat regions; for **blur**, the responses of Laplacian and gradient operators; for **haze**, dark-channel and saturation statistics; for **low light**, global luminance; and for **super-resolution**, the spatial dimensions $H \times W$ of the input. These lightweight global statistics can be computed in a single pass and require no supervision. The resulting vector P_{hints} is then provided to the planner as frequency-aware visual information describing the input degradation.

Instructions and Planning. We consider a low-level restoration task space \mathcal{T} that covers seven representative degradations, including low-light enhancement, dehazing, desnowing, deraining, deblurring, denoising, and super-resolution. In FAPE-IR, Qwen2.5-VL [4] serves as a multimodal planner that turns frequency-aware visual cues and textual instructions into a structured, frequency-explicit restoration plan. Concretely, the planner is conditioned on three types of inputs: a universal restoration instruction r that describes the general goal of recovering a clean and sharp image (details in Appendix 8); an expert rule P_{expert} that encodes the task taxonomy and prior knowledge about which degradations affect which frequency bands (also detailed in Appendix 8); and the concise visual hints P_{hints} derived from the label-free low-level feature pool. Based on these inputs, Qwen2.5-VL produces a parse-friendly textual output, which we then parse into a tuple $FP = (\hat{t}, \hat{f}, \mathcal{R}, \mathcal{E})$, where \hat{t} is the selected task from \mathcal{T} , \hat{f} indicates whether the restoration should primarily focus on high- or low-frequency content, \mathcal{R} summarizes the intended restoration pipeline in natural language, and \mathcal{E} explains the reasoning behind this choice. This human-readable plan acts as a routing signal for downstream high- and low-frequency experts, making the decision process transparent and interpretable even under composite degradations.

Encoding. To ensure the planner’s decisions effectively guide the diffusion-based executor, we use Qwen2.5-VL’s encoding capability to compile the planner decisions FP

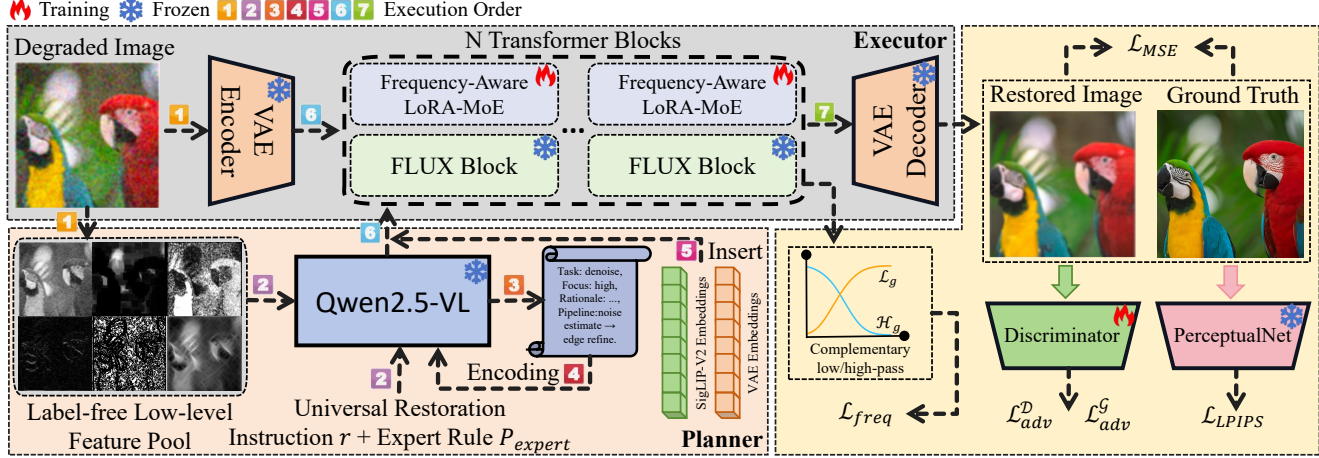


Figure 2. Overview of the proposed FAPE-IR framework.

into compact, frequency-aligned understanding tokens h . To mitigate the gap between understanding tokens and the executor’s generation tokens, we enrich the conditioning tokens with high- and low-frequency visual information. Concretely, we use Qwen2.5-VL’s visual placeholders to inject tokens produced by SigLIP-v2 $\mathcal{E}_{\text{sig}}(c)$ and the VAE $\mathcal{E}_{\text{vae}}(c)$, replacing the executor’s original T5 encoding for conditioning $h_{\text{cond}} = \text{insert}(h, \mathcal{E}_{\text{sig}}(c), \mathcal{E}_{\text{vae}}(c))$. In addition, to retain precise, human-interpretable semantics for the subsequent Frequency-Aware LoRA-MoE module, we similarly use text placeholders to extract the textual tokens $h_{\text{text}} = h[:, \text{slot}_{\text{text}}, :]$.

3.2. Restoration Executor

Given a degraded image c , we employ a restoration executor based on the FLUX transformer [30] to refine the VAE latent z into a restored latent \hat{z} , guided jointly by the textual tokens h_{text} and the conditioning tokens h_{cond} . The VAE decoder then maps \hat{z} to the restored image \hat{x} .

To meet constraints on model size and optimization time, FAPE-IR adopts a parameter-efficient LoRA-MoE executor with two experts specialized for high- and low-frequency bands. Building on this design, we introduce a Frequency-Aware LoRA-MoE module with a dual-end gating mechanism: a planner-side gate uses the frequency-aligned understanding tokens h_{text} to propose an expert selection, while an executor-side gate inspects intermediate high- and low-frequency generation tokens to refine that choice. As illustrated in Figure 3, this design conditions the MoE router jointly on semantic and spectral cues, leading to more precise expert assignment and improved robustness to frequency-band drift during optimization.

3.2.1. Frequency-Aware LoRA-MoE

Frequency-Aware Text Router. Since the planner yields $h_{\text{text}} \in \mathbb{R}^{B \times K \times D}$ while the LoRA-MoE gate operates on $\mathbb{R}^{B \times L \times D}$, we right-pad h_{text} along the token axis to length

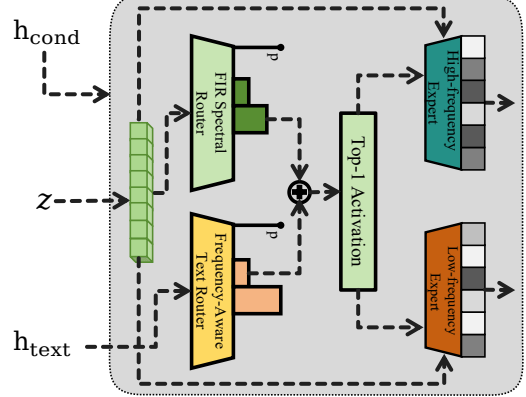


Figure 3. Frequency-Aware LoRA-MoE architecture.

L ($K \leq L$), leaving D unchanged, so that the gating network can be applied token-wise over a sequence of consistent length. Then, we implement the text gating function as a token-wise fully connected layer on the padded text tokens, followed by a softmax over experts to obtain the text gating weights $w_{\text{text}} = \text{Softmax}(W_t \cdot \text{Padding}(h_{\text{text}}))$.

FIR Spectral Router. To compensate for the limitations of high-level semantic tokens in gating, we add a visual-frequency path that separates the executor’s generation tokens into low/high-frequency components using a depthwise FIR low-pass filter [12, 53]. Let $h_{\text{gen}} \in \mathbb{R}^{B \times L \times D}$ denote the per-block input. For an odd kernel size K and a symmetric, normalized 1D Gaussian $g \in \mathbb{R}^K$ with $\sum_k g_k = 1$, we define a depthwise 1D convolution along the token axis as $h_{\text{low}} = \mathcal{L}_g(h_{\text{gen}})$ and $h_{\text{high}} = h_{\text{gen}} - h_{\text{low}}$.

Next, to allocate the proportion of energy between the low- and high-frequency generation tokens, we compute their relative energy and derive the high-low gating weights. Specifically, for each token we set $e_{\text{low}} = \|h_{\text{low}}\|_2^2$ and $e_{\text{high}} = \|h_{\text{high}}\|_2^2$, then $p_{\text{low}} = \frac{e_{\text{low}}}{e_{\text{low}} + e_{\text{high}}}$ and $p_{\text{high}} = 1 - p_{\text{low}}$; a temperature-scaled softmax over $[p_{\text{low}}, p_{\text{high}}]$ yields the high-low gating weights w_{visual} .

Softmax-gated Merged Weights. Subsequently, we fuse the textual and spectral gating weights with non-negative, learnable scalars λ_s : $\tilde{\alpha} = \lambda_s w_{text} + (1 - \lambda_s) w_{visual}$. Finally, we apply top-1 routing to obtain the final frequency-band selection, i.e., $\alpha = \text{Top1}(\tilde{\alpha})$, where α is a one-hot vector indicating the chosen band.

With per-expert coefficients α_i produced by the fused and sparsified router, the FLUX projection is updated as:

$$W' = W + \sum_{i=1}^N \alpha_i A_i B_i, \quad (1)$$

where (A_i, B_i) is a rank- r_i LoRA adapter for the i -th frequency expert and the backbone W is frozen.

3.3. Adversarial Training

To improve efficiency at both training and inference, our FAPE-IR replaces the flow-matching fine-tuning objective [45] commonly used in unified models with adversarial training. In Theorem 6 (Appendix), we show that, compared with auto-regression [74, 77, 89] and flow-matching [9, 17, 40, 95] losses, adversarial training attains fewer artifacts. Next, we detail FAPE-IR’s training paradigm in Figure 2.

Discriminator. Given a ground truth image x (restored image \hat{x}), the frozen SigLIP-v2 discriminator \mathcal{F}_{sig} yields (i) a sequence of hidden states from which we take L token maps at increasing depths and reshape them into spatial feature maps $\{\mathbf{f}^{(l)} \in \mathbb{R}^{C_l \times H_l \times W_l}\}_{l=1}^L$, and (ii) a pooled representation $\mathbf{p} \in \mathbb{R}^D$ from the final layer. To more comprehensively judge the input, we attach a multi-level discriminator head that mines spatial evidence across scales.

Multi-level Discriminator Head. The discriminator head \mathcal{H}_{ψ} processes each spatial map with a shallow, spectrally normalized convolutional path that includes anti-aliasing BlurPool downsampling, and processes the pooled token:

$$\mathbf{s}^{(l)} = \mathcal{H}_{\psi}^{(l)}(\mathbf{f}^{(l)}) \in \mathbb{R}^{H'_l \times W'_l}, s^{\text{pool}} = \mathcal{H}_{\psi}^{\text{pool}}(\mathbf{p}). \quad (2)$$

Each spatial score map $\mathbf{s}^{(l)}$ is spatially averaged to a scalar $\bar{s}^{(l)} = \frac{1}{H'_l W'_l} \sum_{i,j} \mathbf{s}_{ij}^{(l)}$; we then aggregate levelwise with uniform weights: $D(x) = \frac{1}{L+1} \left(\sum_{l=1}^L \bar{s}^{(l)} + s^{\text{pool}} \right)$. This design encourages consistency between local structures (via multi-scale spatial paths) and global semantics (via the pooled path), while remaining lightweight.

Discriminator Loss. Following the adversarial training, we optimize the critic with the standard discriminator loss:

$$\mathcal{L}_{\text{adv}}^D = -\mathbb{E}_x[\log D(x)] - \mathbb{E}_{\hat{x}}[\log(1 - D(\hat{x}))]. \quad (3)$$

Generator Loss. To minimize over-generation and distortion, we do not concatenate additional noise channels into

the inputs of the FLUX transformer. Finally, we train \mathcal{G}_{θ} under a composite adversarial training loss.

$$\mathcal{L}_{\text{adv}} = \underbrace{\alpha \|\hat{x} - x\|_2^2}_{\mathcal{L}_{\text{MSE}}} + \underbrace{\beta \|\phi(\hat{x}) - \phi(x)\|_2^2}_{\mathcal{L}_{\text{LPIPS}}} - \underbrace{\lambda \mathbb{E}[D(\hat{x})]}_{\mathcal{L}_{\text{adv}}^G}. \quad (4)$$

While \mathcal{L}_{adv} promotes pixel fidelity, perceptual similarity, and adversarial realism, it remains agnostic to how spectral content is allocated across experts. To align training with the frequency-aware routing in Subsection 3.1–3.2, we add a single frequency regularizer on adapter outputs that penalizes out-of-band synthesis. This preserves objective parsimony, only one additional scalar term, while explicitly enforcing low/high-band specialization.

Frequency Regularizer. To make the two LoRA–MoE experts specialize in complementary bands, we penalize out-of-band energy on their adapter outputs. Let \mathcal{L}_g be a depthwise FIR low-pass along the token axis, and define its complementary high-pass $\mathcal{H}_g \triangleq I - \mathcal{L}_g$. For the low/high-frequency experts’ outputs y_{low} and y_{high} , we minimize $\mathcal{L}_{\text{freq}} = \text{mean}[\|\mathcal{H}_g(y_{\text{low}})\|_2^2 + \|\mathcal{L}_g(y_{\text{high}})\|_2^2]$. In practice, g is a fixed Gaussian kernel stored as a buffer (non-trainable), and the loss is summed across layers.

At this point, the overall FAPE-IR objective is:

$$\mathcal{L}_{\text{Total}} = \mathcal{L}_{\text{adv}} + \gamma \mathcal{L}_{\text{freq}}. \quad (5)$$

In general, by marrying a frequency-aware planner with band-specialized LoRA–MoE and an adversarial training objective augmented by a single frequency regularizer, our FAPE-IR reconciles interpretability with fidelity.

4. Experiments

4.1. Experimental Setup

Training Data. We construct a training corpus covering seven restoration tasks, including deblurring, dehazing, low-light enhancement, deraining, desnowing, denoising, and super-resolution. Weather-related degradations (deraining, desnowing, dehazing) are sourced from Snow100K-Train [47], Rain100-L/H-Train [104], and the NTIRE 2025 Challenge dataset [37]. For dehazing, we use a curated 10K subset of OTS/ITS-Train [33] combined with URHI-Train [18]. Deblurring utilizes RealBlur-Train (R/J) [64], GoPro-Train, and its gamma-corrected variant [56]. Low-light enhancement is trained on LOL-v2-Train [105]. For denoising, BSD400 [54] and WaterlooED [52] are corrupted with Gaussian noise at $\sigma \in \{15, 25, 50\}$. For super-resolution, we follow prior work [92, 97, 98] and adopt LS-DIR [38] plus a 10K-image FFHQ subset [27], with degradations synthesized via Real-ESRGAN [88].

Testing Data. We evaluate our method on a comprehensive collection of benchmarks that span both synthetic and real-world degradations across deblurring, dehazing, low-light

Table 1. Unified comparison across six AIO-IR task series. Each series shows five metrics (PSNR↑, SSIM↑, LPIPS↓, FID↓, DISTs↓). The best results are highlighted in red, and the second-best results are shown in blue.

Method	Deraining					Denoising					Deblurring				
	PSNR↑	SSIM↑	LPIPS↓	FID↓	DISTs↓	PSNR↑	SSIM↑	LPIPS↓	FID↓	DISTs↓	PSNR↑	SSIM↑	LPIPS↓	FID↓	DISTs↓
PromptIR [58]	21.94	0.73	0.30	100.17	0.21	31.27	0.84	0.16	57.82	0.14	—	—	—	—	—
FoundIR [34]	19.68	0.68	0.37	118.29	0.24	30.85	0.80	0.21	67.08	0.22	28.35	0.85	0.21	42.03	0.16
DFPIR [78]	19.27	0.68	0.37	104.13	0.27	31.31	0.83	0.17	61.80	0.15	30.82	0.90	0.15	28.23	0.12
MoCE-IR [109]	21.42	0.71	0.32	101.21	0.23	31.63	0.84	0.16	56.74	0.14	21.67	0.74	0.28	48.85	0.19
AdaIR [15]	21.64	0.71	0.32	100.07	0.23	31.45	0.84	0.17	58.05	0.14	22.23	0.75	0.28	49.64	0.19
FAPE-IR (Ours)	28.30	0.84	0.09	21.55	0.07	30.34	0.87	0.10	30.33	0.09	30.91	0.88	0.10	16.53	0.07
Method	Desnowing					Dehazing					Low-light enhancement				
	PSNR↑	SSIM↑	LPIPS↓	FID↓	DISTs↓	PSNR↑	SSIM↑	LPIPS↓	FID↓	DISTs↓	PSNR↑	SSIM↑	LPIPS↓	FID↓	DISTs↓
PromptIR [58]	—	—	—	—	—	21.94	0.90	0.14	24.26	0.11	—	—	—	—	—
FoundIR [34]	23.79	0.78	0.28	29.31	0.17	13.65	0.75	0.31	34.41	0.21	14.44	0.67	0.32	86.46	0.22
DFPIR [78]	20.78	0.74	0.30	34.86	0.18	13.54	0.73	0.30	29.43	0.21	25.92	0.90	0.16	52.15	0.13
MoCE-IR [109]	23.82	0.76	0.28	30.47	0.16	15.54	0.80	0.22	27.98	0.15	23.36	0.89	0.16	44.61	0.12
AdaIR [15]	24.19	0.77	0.27	26.82	0.16	19.89	0.88	0.16	25.71	0.12	24.51	0.86	0.17	50.78	0.13
FAPE-IR (Ours)	30.29	0.88	0.08	1.49	0.06	33.85	0.97	0.04	7.21	0.04	25.34	0.90	0.11	40.30	0.09

Table 2. Unified comparison across SR task series. Each series shows five metrics. The best results are marked in red, and the second-best results are shown in blue.

Method	SR				
	PSNR↑	SSIM↑	LPIPS↓	FID↓	DISTs↓
StableSR [83]	25.10	0.73	0.29	110.18	0.22
DiffBIR [41]	25.65	0.65	0.39	124.53	0.25
SeeSR [98]	26.60	0.74	0.31	122.10	0.23
PASD [103]	26.87	0.75	0.29	120.46	0.21
OSEDiff [97]	26.49	0.76	0.28	117.55	0.21
PURE [92]	24.47	0.64	0.38	121.07	0.24
FAPE-IR (Ours)	28.53	0.85	0.19	85.82	0.15

enhancement, deraining, desnowing, denoising, and super-resolution. For deblurring, we adopt the official test splits of RealBlur-J/R [64], GoPro, and GoPro_gamma [56]. Dehazing evaluation is conducted using the ITS validation set and the URHI test split [33]. Low-light enhancement is assessed on the test sets of LOL-v1 [91] and LOL-v2 [105]. Deraining is benchmarked on Rain100-L/H [104], OutDoor [35], and RainDrop [60]. For desnowing, we use the Snow100K-L and Snow100K-S test subsets [47] for large-scale qualitative comparison. Denoising performance is measured on BSD68 [54] and Urban100 [22], each corrupted with additive Gaussian noise at $\sigma \in \{15, 25, 50\}$. Super-resolution is evaluated on RealSR [26] and DRealSR [93] at $\times 2$ and $\times 4$ scales. We follow standard evaluation protocols: RealSR is tested using the center-crop strategy [92], while images from other benchmarks are resized to 512×512 .

Optimization. We train our FAPE-IR framework using the Prodigy optimizer [55] for the main model and AdamW [48] for the discriminator head. The base learning rate for AdamW is initialized at 1.0 and cosine-annealed during training. All models are trained for 200K steps with a batch size of 1 on 512×512 inputs across all datasets. Training is conducted on 8× NVIDIA H200 GPUs. In the

Table 3. Complexity comparison. All methods are evaluated on 512×512 inputs, and inference is measured on an H200 GPU.

Metric	Methods					
	FoundIR [34]	DFPIR [78]	MoCE-IR [109]	AdaIR [15]	PURE [92]	Ours
Time (s)	0.18	0.08	0.10	0.10	201.67	1.57
Param (G)	3.36	3.92	2.11	3.49	26.22	38.92

one-step setting, we use $\alpha = 50.0$, $\beta = 5.0$, $\lambda = 0.5$, $\gamma = 1 \times 10^{-3}$, and a diffusion timestep $t = 300$.

4.2. Quantitative Results

We conduct a quantitative comparison between FAPE-IR and recent AIO-IR methods, including PromptIR [58] (NeurIPS’23), FoundIR [34] (ICCV’25), AdaIR [15] (ICLR’25), DFPIR [78] (CVPR’25), and MoCE-IR [109] (CVPR’25), as well as some SR methods: StableSR [83] (IJCV’24), DiffBIR [41] (ECCV’24), SeeSR [98] (CVPR’24), PASD [103] (ECCV’24), OSEDiff [97] (NeurIPS’24), and PURE [92] (ICCV’25). *We evaluate all tasks on a single trained model rather than training for each task and testing them individually.*

As summarized in Table 1 and Table 2 (with per-benchmark scores and perceptual metrics detailed in Table 5 and Table 6 in the Appendix), FAPE-IR consistently secures either the best or second-best results across all six AIO-IR task series. On weather-related benchmarks (deraining, desnowing, dehazing), FAPE-IR brings substantial gains over the strongest baselines, typically improving PSNR by about 6–8 dB and reducing perceptual distances (LPIPS, FID, DISTs) by several times (e.g., deraining improves PSNR from 21.94 dB to 28.30 dB and FID from around 100.07 to 21.55). These improvements are most evident on degradations with rich semantic layouts and complex frequency patterns, where the frequency-aware planner guides the LoRA-MoE executor to apply band-specialized experts, yielding cleaner structures and fewer artifacts. For denois-



Figure 4. Comparison among unified models, including BAGEL [17], Nexus-Gen [111], Uniworld-V1 [40], and Emu3.5 [16].

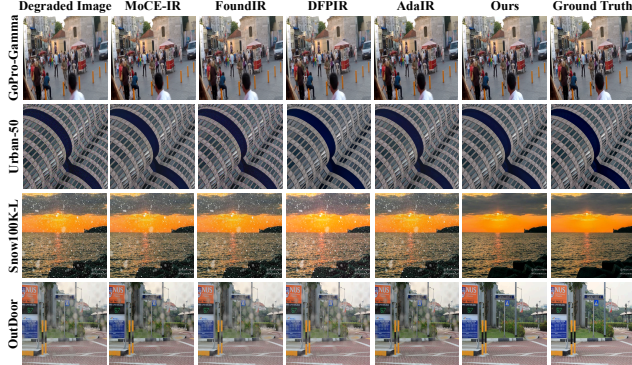


Figure 5. High-frequency-dominant tasks (derain/desnow/de-blur/denoise): FAPE-IR preserves fine structures and textures with less ringing/oversharpening. Please zoom in for details.

ing and low-light enhancement, FAPE-IR attains slightly lower PSNR than the best methods but achieves the best SSIM and consistently lower LPIPS/FID/DISTS, suggesting that the combination of frequency-aware planning and adversarial training favors perceptually faithful details. On SR benchmarks, FAPE-IR again outperforms all competitors on all five metrics, for instance increasing PSNR from 26.87 dB to 28.53 dB and SSIM from 0.76 to 0.85 while notably reducing FID and DISTS, indicating that our FAPE-IR performs well on mixed degradations. Overall, these results show that explicitly modeling both semantic structure and frequency content allows FAPE-IR to strike a strong balance between distortion and perceptual quality across a broad range of degradations.

To meet real-world latency requirements, Table 3 further shows that, despite its larger number of parameters, FAPE-IR maintains reasonable inference time and runs notably faster than the unified counterpart PURE [92], suggesting that the framework is feasible for interactive applications.

4.3. Visual Comparison with Unified Models

As shown in Figure 4, we benchmark FAPE-IR against recent unified models on low-level restoration. On RainDrop, most unified models lack explicit low-level modeling and thus fail to complete restoration, either removing only a subset of droplets or causing noticeable color shifts. Emu 3.5 [16] shows a marked jump over earlier Emu variants [73, 74, 89] and contemporaries like BAGEL [17], Uniworld-V1 [40], and Nexus-Gen [111], likely due to its

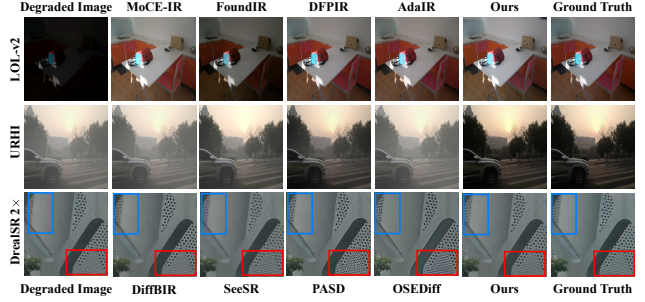


Figure 6. Low-frequency & SR: FAPE-IR cleans haze and balances illumination, preserving color; for SR it yields higher fidelity and fewer artifacts. Please zoom in for details.

large corpus and 34.1B parameters. However, its multi-modal autoregression design still introduces fine-detail artifacts. By contrast, FAPE-IR reliably restores structures without color drift, underscoring the benefits of frequency-aware planning and band-specialized execution, and pointing toward a path to transfer it to future unified models.

4.4. Visual Comparison with AIO-IR Models

As shown in Figure 5 and Figure 6, we provide visual comparisons between FAPE-IR and prior AIO-IR methods. Relative to contemporaries, FAPE-IR exhibits stronger visual robustness. In high-frequency tasks, on the large-scale Snow100K-L/S benchmarks, competing methods often fail to recover fine structures, whereas FAPE-IR reconstructs them faithfully. On Urban-50, although a few methods achieve slightly higher scores, FAPE-IR produces visibly less noise and cleaner edges. In low-frequency cases, such as URHI, most baselines restore only portions of the scene, while FAPE-IR more completely removes the haze veil and corrects illumination. For super-resolution, FAPE-IR maintains the highest fidelity to GT with fewer artifacts, preserving textures and text without over-sharpening. These observations are consistent with the quantitative trends. Overall, FAPE-IR suppresses artifacts robustly, maintains strong pixel anchoring, and improves the realism of fine details.

4.5. Ablation Study

Under a controlled setting where we fix all hyperparameters and train for only 10K steps, we perform a minimal ablation of the frequency-aware pipeline. As shown in Table 4, on URHI (low-frequency / haze-dominant), the baseline without Qwen, Freq-U, or Freq-G reaches only

Table 4. Ablation on URHI benchmark. Qwen: remove Qwen2.5-VL; Freq-U: remove frequency-aware text router; Freq-G: remove FIR spectral router; r : expert combos.

Qwen	Freq-U	Freq-G	$r=4$	$r=8$	$r=16$	PSNR \uparrow	SSIM \uparrow
\times	\times	\times		\checkmark		25.03	0.92
\checkmark	\times	\times		\checkmark		27.95	0.94
+ Freq-U enabled							
\checkmark	\checkmark	\times		\checkmark		28.92	0.94
\checkmark	\checkmark	\times		\checkmark		28.89	0.95
\checkmark	\checkmark	\times	\checkmark		\checkmark	24.75	0.91
\checkmark	\checkmark	\times		\checkmark	\checkmark	24.77	0.92
+ Freq-G enabled							
\checkmark	\checkmark	\checkmark		\checkmark		29.71	0.95
\checkmark	\checkmark	\checkmark		\checkmark		25.93	0.93
\checkmark	\checkmark	\checkmark		\checkmark	\checkmark	29.60	0.95

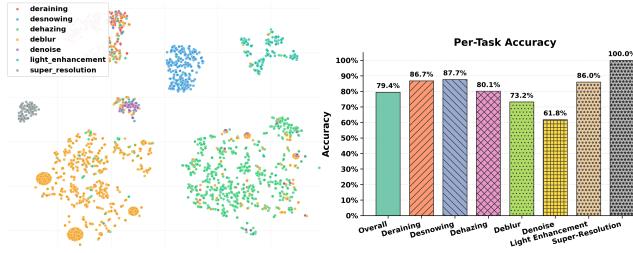


Figure 7. Low-level task planning. (a) The frequency-aware planner yields separable, spectrum-aligned manifolds in feature space using only its own hidden states. (b) Text-based task classification accuracy of Qwen2.5-VL on the corresponding tasks.

25.03 dB / 0.92 SSIM. Simply adding Qwen2.5-VL without any routing control improves performance to 27.95 dB / 0.94 SSIM, indicating that semantic planning is beneficial but insufficient to yield effective compute allocation. Coupling planner outputs to the MoE gate (Freq-U) further stabilizes performance at around 28.9 dB / 0.94–0.95 SSIM, showing that the model can already autonomously perceive and select frequency bands. Injecting token-derived spectral priors into the gate (Freq-G) yields the best result of 29.71 dB / 0.95 SSIM, corresponding to a +4.68 dB PSNR gain over the no-planner baseline and noticeably more consistent behavior across configurations.

We also study the impact of LoRA–MoE capacity (r) and expert allocation. With no frequency priors, a balanced capacity (8/8) is the most stable. Under the Freq-G constraint, a mildly asymmetric allocation (8/16), aligned with the planner-indicated dominant band, maintains near-optimal performance (29.60 dB). In contrast, extremely skewed settings (4/16) degrade performance both with and without priors (down to 25.93 / 24.75 dB), suggesting that simply reshaping the LoRA structure is insufficient to disentangle frequency bands. Instead, the coupling of frequency priors with semantic planning is key to achieving stable routing and overall performance gains.

4.6. Low-Level Task Planning

We assess whether the planner’s decisions form a task- and frequency-aware representation that is both separa-



Figure 8. Frequency-aware planner outputs. We visualize results on representative corrupted inputs covering four tasks.

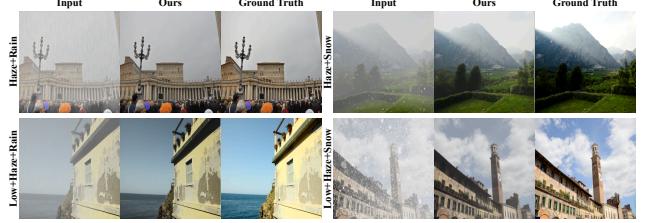


Figure 9. Compound degradations (haze+rain/snow; low-light mixtures): FAPE-IR removes low-frequency artifacts, preserves details, and reduces cross-artifacts. Please zoom in for details.

ble and useful. Specifically, we freeze the Qwen2.5-VL planner, extract the decision token sequence FP for each input (BSD68-50, URHI, GoPro, LOL-v2, RainDrop, Snow100K-S, RealSR $\times 2$), and mean-pool their final-layer states. The resulting t-SNE embedding (Figure 7) exhibits clean, task-dependent manifolds. Nevertheless, the text-based task readout achieves 79.4% accuracy overall (all images in BSD68-50 are grayscale, which can spuriously trigger low-light flags). Moreover, the exemplars (Figure 8) show that the planner’s outputs not only describe but also instantiate a causal frequency control path for restoration. Collectively, these analyses demonstrate that the planner provides interpretable, frequency-aligned, and causally effective signals that steer band-specialized restoration, explaining the sharper, artifact-averse behavior.

4.7. Generalization to Multi-Degradation Tasks

To assess generalization beyond single degradations, we evaluate FAPE-IR on the recent CDD-11 benchmark [21], which contains real-world images with multi-degradation tasks. As shown in Figure 9, although FAPE-IR is trained exclusively on single-degradation data, it exhibits strong out-of-distribution performance on these compound mixtures, indicating a non-trivial level of degradation-agnostic generalization. We attribute this to the frequency-aware LoRA-MoE module, which in a single forward pass dispatches complementary experts, allocating low-frequency capacity to illumination correction and veil removal while activating high-frequency capacity around edges and fine textures, consistent with the layered nature of degradations. Overall, the results substantiate FAPE-IR’s robustness and its ability to generalize to unseen composite degradations.

5. Conclusion

We introduce FAPE-IR, a unified AIO-IR framework that couples an interpretable, frequency-aware planner with a diffusion-based executor equipped with the frequency-aware LoRA-MoE module, trained under the adversarial training objective with a single frequency regularizer. By making the semantics–spectrum link explicit, FAPE-IR improves cross-task disentanglement and sharing, stabilizes optimization, and improves open-world robustness. It achieves state-of-the-art or competitive performance across seven AIO-IR tasks and shows strong zero-shot generalization on unseen composite degradations.

References

- [1] Yuang Ai, Huaibo Huang, Xiaoqiang Zhou, Jieyang Wang, and Ran He. Multimodal prompt perceiver: Empower adaptiveness generalizability and fidelity for all-in-one image restoration. In *Proceedings of the IEEE/CVF Conference on Computer Vision and Pattern Recognition*, pages 25432–25444, 2024. 1
- [2] Luigi Ambrosio, Elia Brué, Daniele Semola, et al. *Lectures on optimal transport*. Springer, 2021. 1, 6, 7, 8
- [3] Martin Arjovsky, Soumith Chintala, and Léon Bottou. Wasserstein generative adversarial networks. In *International conference on machine learning*, pages 214–223. PMLR, 2017. 1, 6, 8
- [4] Shuai Bai, Keqin Chen, Xuejing Liu, Jialin Wang, Wenbin Ge, Sibo Song, Kai Dang, Peng Wang, Shijie Wang, Jun Tang, et al. Qwen2. 5-vl technical report. *arXiv preprint arXiv:2502.13923*, 2025. 3
- [5] Samy Bengio, Oriol Vinyals, Navdeep Jaitly, and Noam Shazeer. Scheduled sampling for sequence prediction with recurrent neural networks. *Advances in neural information processing systems*, 28, 2015. 4, 8
- [6] Ashish Bora, Ajil Jalal, Eric Price, and Alexandros G Dimakis. Compressed sensing using generative models. In *International conference on machine learning*, pages 537–546. PMLR, 2017. 1, 6
- [7] Haowei Chen, Zhiwen Yang, Haotian Hou, Hui Zhang, Bingzheng Wei, Gang Zhou, and Yan Xu. All-in-one medical image restoration with latent diffusion-enhanced vector-quantized codebook prior. In *International Conference on Medical Image Computing and Computer-Assisted Intervention*, pages 67–77. Springer, 2025. 1
- [8] I Chen, Wei-Ting Chen, Yu-Wei Liu, Yuan-Chun Chiang, Sy-Yen Kuo, Ming-Hsuan Yang, et al. Unirestore: Unified perceptual and task-oriented image restoration model using diffusion prior. In *Proceedings of the Computer Vision and Pattern Recognition Conference*, pages 17969–17979, 2025. 1, 2
- [9] Juhai Chen, Zhiyang Xu, Xichen Pan, Yushi Hu, Can Qin, Tom Goldstein, Lifu Huang, Tianyi Zhou, Saining Xie, Silvio Savarese, et al. Blip3-o: A family of fully open unified multimodal models-architecture, training and dataset. *arXiv preprint arXiv:2505.09568*, 2025. 2, 3, 5
- [10] Xiangyu Chen, Yihao Liu, Yuandong Pu, Wenlong Zhang, Jiantao Zhou, Yu Qiao, and Chao Dong. Learning a low-level vision generalist via visual task prompt. In *Proceedings of the 32nd ACM International Conference on Multimedia*, pages 2671–2680, 2024. 1
- [11] Xiangyu Chen, Kaiwen Zhu, Yuandong Pu, Shuo Cao, Xiaohui Li, Wenlong Zhang, Yihao Liu, Yu Qiao, Jiantao Zhou, and Chao Dong. Exploring scalable unified modeling for general low-level vision. *arXiv preprint arXiv:2507.14801*, 2025. 1
- [12] Yunpeng Chen, Haoqi Fan, Bing Xu, Zhicheng Yan, Yannis Kalantidis, Marcus Rohrbach, Shuicheng Yan, and Jiasi Feng. Drop an octave: Reducing spatial redundancy in convolutional neural networks with octave convolution. In *Proceedings of the IEEE/CVF international conference on computer vision*, pages 3435–3444, 2019. 4
- [13] Zihan Cheng, Liangtai Zhou, Dian Chen, Ni Tang, Xiaotong Luo, and Yanyun Qu. Unildiff: Unlocking the power of diffusion priors for all-in-one image restoration. *arXiv preprint arXiv:2507.23685*, 2025. 2
- [14] Marcos V Conde, Gregor Geigle, and Radu Timofte. Instructir: High-quality image restoration following human instructions. In *European Conference on Computer Vision*, pages 1–21. Springer, 2024. 2
- [15] Yuning Cui, Syed Waqas Zamir, Salman Khan, Alois Knoll, Mubarak Shah, and Fahad Shahbaz Khan. Adair: Adaptive all-in-one image restoration via frequency mining and modulation. *arXiv preprint arXiv:2403.14614*, 2024. 2, 6, 9, 10, 11
- [16] Yufeng Cui, Honghao Chen, Haoge Deng, Xu Huang, Xinghang Li, Jirong Liu, Yang Liu, Zhuoyan Luo, Jinseng Wang, Wenxuan Wang, et al. Emu3. 5: Native multimodal models are world learners. *arXiv preprint arXiv:2510.26583*, 2025. 7, 12
- [17] Chaorui Deng, Deyao Zhu, Kunchang Li, Chenhui Gou, Feng Li, Zeyu Wang, Shu Zhong, Weihao Yu, Xiaonan Nie, Ziang Song, et al. Emerging properties in unified multimodal pretraining. *arXiv preprint arXiv:2505.14683*, 2025. 2, 3, 5, 7, 12
- [18] Chengyu Fang, Chunming He, Fengyang Xiao, Yulun Zhang, Longxiang Tang, Yuelin Zhang, Kai Li, and Xiu Li. Real-world image dehazing with coherence-based pseudo labeling and cooperative unfolding network. *Advances in Neural Information Processing Systems*, 37:97859–97883, 2024. 5
- [19] David J Field. Relations between the statistics of natural images and the response properties of cortical cells. *Journal of the Optical Society of America A*, 4(12):2379–2394, 1987. 1
- [20] Jinpei Guo, Zheng Chen, Wenbo Li, Yong Guo, and Yulun Zhang. Compression-aware one-step diffusion model for jpeg artifact removal. *arXiv preprint arXiv:2502.09873*, 2025. 1
- [21] Yu Guo, Yuan Gao, Yuxu Lu, Huilin Zhu, Ryan Wen Liu, and Shengfeng He. Onerestore: A universal restoration framework for composite degradation. In *European conference on computer vision*, pages 255–272. Springer, 2024. 8

[22] Jia-Bin Huang, Abhishek Singh, and Narendra Ahuja. Single image super-resolution from transformed self-exemplars. In *Proceedings of the IEEE conference on computer vision and pattern recognition*, pages 5197–5206, 2015. 6

[23] Aapo Hyvärinen and Peter Dayan. Estimation of non-normalized statistical models by score matching. *Journal of Machine Learning Research*, 6(4), 2005. 1, 6, 8

[24] Aapo Hyvärinen, Jarmo Hurri, and Patrick O Hoyer. *Natural image statistics: A probabilistic approach to early computational vision*. Springer Science & Business Media, 2009. 1

[25] Yuhwan Jeong, Yunseo Yang, Youngho Yoon, and Kuk-Jin Yoon. Robust adverse weather removal via spectral-based spatial grouping. In *Proceedings of the IEEE/CVF International Conference on Computer Vision*, pages 11872–11883, 2025. 1

[26] Xiaozhong Ji, Yun Cao, Ying Tai, Chengjie Wang, Jilin Li, and Feiyue Huang. Real-world super-resolution via kernel estimation and noise injection. In *proceedings of the IEEE/CVF conference on computer vision and pattern recognition workshops*, pages 466–467, 2020. 6

[27] Tero Karras, Samuli Laine, and Timo Aila. A style-based generator architecture for generative adversarial networks. In *Proceedings of the IEEE/CVF conference on computer vision and pattern recognition*, pages 4401–4410, 2019. 5

[28] Bahjat Kawar, Michael Elad, Stefano Ermon, and Jiaming Song. Denoising diffusion restoration models. *Advances in neural information processing systems*, 35:23593–23606, 2022. 1

[29] Dilip Krishnan and Rob Fergus. Fast image deconvolution using hyper-laplacian priors. *Advances in neural information processing systems*, 22, 2009. 1

[30] Black Forest Labs. Flux. <https://github.com/black-forest-labs/flux>, 2024. 2, 4

[31] Guanzhou Lan, Qianli Ma, Yuqi Yang, Zhigang Wang, Dong Wang, Xuelong Li, and Bin Zhao. Efficient diffusion as low light enhancer. In *Proceedings of the Computer Vision and Pattern Recognition Conference*, pages 21277–21286, 2025. 1

[32] Anat Levin, Yair Weiss, Fredo Durand, and William T Freeman. Understanding and evaluating blind deconvolution algorithms. In *2009 IEEE conference on computer vision and pattern recognition*, pages 1964–1971. IEEE, 2009. 1

[33] Boyi Li, Wenqi Ren, Dengpan Fu, Dacheng Tao, Dan Feng, Wenjun Zeng, and Zhangyang Wang. Benchmarking single-image dehazing and beyond. *IEEE transactions on image processing*, 28(1):492–505, 2018. 5, 6

[34] Hao Li, Xiang Chen, Jiangxin Dong, Jinhui Tang, and Jinshan Pan. Foundir: Unleashing million-scale training data to advance foundation models for image restoration. In *ICCV*, 2025. 6, 9, 10, 11

[35] Ruoteng Li, Loong-Fah Cheong, and Robby T Tan. Heavy rain image restoration: Integrating physics model and conditional adversarial learning. In *Proceedings of the IEEE/CVF conference on computer vision and pattern recognition*, pages 1633–1642, 2019. 6

[36] Shufan Li, Konstantinos Kallidromitis, Hritik Bansal, Akash Gokul, Yusuke Kato, Kazuki Kozuka, Jason Kuen, Zhe Lin, Kai-Wei Chang, and Aditya Grover. Lavida: A large diffusion language model for multimodal understanding. *arXiv preprint arXiv:2505.16839*, 2025. 3

[37] Xin Li, Yeying Jin, Xin Jin, Zongwei Wu, Bingchen Li, Yufei Wang, Wenhan Yang, Yu Li, Zhibo Chen, Bihan Wen, et al. Ntire 2025 challenge on day and night raindrop removal for dual-focused images: Methods and results. In *Proceedings of the Computer Vision and Pattern Recognition Conference*, pages 1172–1183, 2025. 5

[38] Yawei Li, Kai Zhang, Jingyun Liang, Jiezhang Cao, Ce Liu, Rui Gong, Yulun Zhang, Hao Tang, Yun Liu, Denis Demandolx, et al. Lsdir: A large scale dataset for image restoration. In *Proceedings of the IEEE/CVF Conference on Computer Vision and Pattern Recognition*, pages 1775–1787, 2023. 5

[39] Zilong Li, Yiming Lei, Chenglong Ma, Junping Zhang, and Hongming Shan. Prompt-in-prompt learning for universal image restoration. *arXiv preprint arXiv:2312.05038*, 2023. 1, 2

[40] Bin Lin, Zongjian Li, Xinhua Cheng, Yuwei Niu, Yang Ye, Xianyi He, Shenghai Yuan, Wangbo Yu, Shaodong Wang, Yunyang Ge, et al. Uniworld: High-resolution semantic encoders for unified visual understanding and generation. *arXiv preprint arXiv:2506.03147*, 2025. 2, 3, 5, 7, 12

[41] Xinqi Lin, Jingwen He, Ziyan Chen, Zhaoyang Lyu, Bo Dai, Fanghua Yu, Yu Qiao, Wanli Ouyang, and Chao Dong. Diffbir: Toward blind image restoration with generative diffusion prior. In *European conference on computer vision*, pages 430–448. Springer, 2024. 6, 9, 10, 11

[42] Yunlong Lin, Zixu Lin, Haoyu Chen, Panwang Pan, Chenxin Li, Sixiang Chen, Kairun Wen, Yeying Jin, Wenbo Li, and Xinghao Ding. Jarvisir: Elevating autonomous driving perception with intelligent image restoration. In *Proceedings of the Computer Vision and Pattern Recognition Conference*, pages 22369–22380, 2025. 1

[43] Tony Lindeberg. Feature detection with automatic scale selection. *International journal of computer vision*, 30(2):79–116, 1998. 1

[44] Torgny Lindvall. *Lectures on the coupling method*. Courier Corporation, 2002. 8

[45] Yaron Lipman, Ricky TQ Chen, Heli Ben-Hamu, Maximilian Nickel, and Matt Le. Flow matching for generative modeling. *arXiv preprint arXiv:2210.02747*, 2022. 5, 1, 8, 13

[46] Xingchao Liu, Chengyue Gong, and Qiang Liu. Flow straight and fast: Learning to generate and transfer data with rectified flow. *arXiv preprint arXiv:2209.03003*, 2022. 1, 8

[47] Yun-Fu Liu, Da-Wei Jaw, Shih-Chia Huang, and Jenq-Neng Hwang. Desnownet: Context-aware deep network for snow removal. *IEEE Transactions on Image Processing*, 27(6):3064–3073, 2018. 5, 6

[48] Ilya Loshchilov and Frank Hutter. Decoupled weight decay regularization. *arXiv preprint arXiv:1711.05101*, 2017. 6

[49] Wenyang Luo, Haina Qin, Zewen Chen, Libin Wang, Dandan Zheng, Yuming Li, Yufan Liu, Bing Li, and Weiming

Hu. Visual-instructed degradation diffusion for all-in-one image restoration. In *Proceedings of the Computer Vision and Pattern Recognition Conference*, pages 12764–12777, 2025. 1

[50] Ziwei Luo, Fredrik K Gustafsson, Zheng Zhao, Jens Sjölund, and Thomas B Schön. Controlling vision-language models for universal image restoration. *arXiv preprint arXiv:2310.01018*, 3(8), 2023. 1, 2

[51] Jiaqi Ma, Tianheng Cheng, Guoli Wang, Qian Zhang, Xinggang Wang, and Lefei Zhang. Prores: Exploring degradation-aware visual prompt for universal image restoration. *arXiv preprint arXiv:2306.13653*, 2023. 1, 2

[52] Kede Ma, Zhengfang Duanmu, Qingbo Wu, Zhou Wang, Hongwei Yong, Hongliang Li, and Lei Zhang. Waterloo exploration database: New challenges for image quality assessment models. *IEEE Transactions on Image Processing*, 26(2):1004–1016, 2016. 5

[53] Aziz Makandar and Bhagirathi Halalli. Image enhancement techniques using highpass and lowpass filters. *International Journal of Computer Applications*, 109(14), 2015. 4

[54] David Martin, Charless Fowlkes, Doron Tal, and Jitendra Malik. A database of human segmented natural images and its application to evaluating segmentation algorithms and measuring ecological statistics. In *Proceedings eighth IEEE international conference on computer vision. ICCV 2001*, pages 416–423. IEEE, 2001. 5, 6

[55] Konstantin Mishchenko and Aaron Defazio. Prodigy: An expeditiously adaptive parameter-free learner. *arXiv preprint arXiv:2306.06101*, 2023. 6

[56] Seungjun Nah, Tae Hyun Kim, and Kyoung Mu Lee. Deep multi-scale convolutional neural network for dynamic scene deblurring. In *Proceedings of the IEEE conference on computer vision and pattern recognition*, pages 3883–3891, 2017. 5, 6

[57] Vaishnav Potlapalli, Syed Waqas Zamir, Salman Khan, and Fahad Khan. Promptir: Prompting for all-in-one image restoration. In *Thirty-seventh Conference on Neural Information Processing Systems*, 2023. 1, 2

[58] Vaishnav Potlapalli, Syed Waqas Zamir, Salman Khan, and Fahad Khan. Promptir: Prompting for all-in-one image restoration. In *Advances in Neural Information Processing Systems*, 2023. 2, 6, 9, 10, 11

[59] Yuandong Pu, Le Zhuo, Kaiwen Zhu, Liangbin Xie, Wenlong Zhang, Xiangyu Chen, Peng Gao, Yu Qiao, Chao Dong, and Yihao Liu. Lumina-omniv: A unified multimodal framework for general low-level vision. *arXiv preprint arXiv:2504.04903*, 2025. 1

[60] Rui Qian, Robby T Tan, Wenhan Yang, Jiajun Su, and Jiaying Liu. Attentive generative adversarial network for raindrop removal from a single image. In *Proceedings of the IEEE conference on computer vision and pattern recognition*, pages 2482–2491, 2018. 6

[61] Alec Radford, Jong Wook Kim, Chris Hallacy, Aditya Ramesh, Gabriel Goh, Sandhini Agarwal, Girish Sastry, Amanda Askell, Pamela Mishkin, Jack Clark, et al. Learning transferable visual models from natural language supervision. In *International conference on machine learning*, pages 8748–8763. PMLR, 2021. 2

[62] Marc’Aurelio Ranzato, Sumit Chopra, Michael Auli, and Wojciech Zaremba. Sequence level training with recurrent neural networks. *arXiv preprint arXiv:1511.06732*, 2015. 4, 8

[63] Mengwei Ren, Mauricio Delbracio, Hossein Talebi, Guido Gerig, and Peyman Milanfar. Multiscale structure guided diffusion for image deblurring. In *Proceedings of the IEEE/CVF International Conference on Computer Vision*, pages 10721–10733, 2023. 1

[64] Jaesung Rim, Haeyun Lee, Juchol Won, and Sunghyun Cho. Real-world blur dataset for learning and benchmarking deblurring algorithms. In *European conference on computer vision*, pages 184–201. Springer, 2020. 5, 6

[65] Yaniv Romano, Michael Elad, and Peyman Milanfar. The little engine that could: Regularization by denoising (red). *SIAM journal on imaging sciences*, 10(4):1804–1844, 2017. 1, 6

[66] Stéphane Ross, Geoffrey Gordon, and Drew Bagnell. A reduction of imitation learning and structured prediction to no-regret online learning. In *Proceedings of the fourteenth international conference on artificial intelligence and statistics*, pages 627–635. JMLR Workshop and Conference Proceedings, 2011. 4, 8

[67] Daniel Ruderman and William Bialek. Statistics of natural images: Scaling in the woods. *Advances in neural information processing systems*, 6, 1993. 1

[68] Zhenning Shi, Chen Xu, Changsheng Dong, Bin Pan, Along He, Tao Li, Huazhu Fu, et al. Resfusion: Denoising diffusion probabilistic models for image restoration based on prior residual noise. *Advances in Neural Information Processing Systems*, 37:130664–130693, 2024. 1

[69] Eero P Simoncelli and Bruno A Olshausen. Natural image statistics and neural representation. *Annual review of neuroscience*, 24(1):1193–1216, 2001. 1

[70] Yang Song, Jascha Sohl-Dickstein, Diederik P Kingma, Abhishek Kumar, Stefano Ermon, and Ben Poole. Score-based generative modeling through stochastic differential equations. *arXiv preprint arXiv:2011.13456*, 2020. 1, 6, 8

[71] Jon Sporrings, Mads Nielsen, Luc Florack, and Peter Johansen. *Gaussian scale-space theory*. Springer Science & Business Media, 2013. 1

[72] Bharath K Sriperumbudur, Kenji Fukumizu, Arthur Gretton, Bernhard Schölkopf, and Gert RG Lanckriet. On integral probability metrics, ϕ -divergences and binary classification. *arXiv preprint arXiv:0901.2698*, 2009. 1, 6, 8

[73] Quan Sun, Qiying Yu, Yufeng Cui, Fan Zhang, Xiaosong Zhang, Yueze Wang, Hongcheng Gao, Jingjing Liu, Tiejun Huang, and Xinlong Wang. Emu: Generative pretraining in multimodality. *arXiv preprint arXiv:2307.05222*, 2023. 7

[74] Quan Sun, Yufeng Cui, Xiaosong Zhang, Fan Zhang, Qiying Yu, Yueze Wang, Yongming Rao, Jingjing Liu, Tiejun Huang, and Xinlong Wang. Generative multimodal models are in-context learners. In *Proceedings of the IEEE/CVF Conference on Computer Vision and Pattern Recognition*, pages 14398–14409, 2024. 5, 7

[75] Alexander Swerdlow, Mihir Prabhudesai, Siddharth Gandhi, Deepak Pathak, and Katerina Fragkiadaki.

Unified multimodal discrete diffusion. *arXiv preprint arXiv:2503.20853*, 2025. 3

[76] Hongxuan Tang, Hao Liu, and Xinyan Xiao. Ugen: Unified autoregressive multimodal model with progressive vocabulary learning. *arXiv preprint arXiv:2503.21193*, 2025. 3

[77] Chameleon Team. Chameleon: Mixed-modal early-fusion foundation models. *arXiv preprint arXiv:2405.09818*, 2024. 3, 5

[78] Xiangpeng Tian, Xiangyu Liao, Xiao Liu, Meng Li, and Chao Ren. Degradation-aware feature perturbation for all-in-one image restoration. In *Proceedings of the Computer Vision and Pattern Recognition Conference*, pages 28165–28175, 2025. 1, 2, 6, 9, 10, 11

[79] Michael Tschannen, Alexey Gritsenko, Xiao Wang, Muhammad Ferjad Naeem, Ibrahim Alabdulmohsin, Nikhil Parthasarathy, Talfan Evans, Lucas Beyer, Ye Xia, Basil Mustafa, et al. Siglip 2: Multilingual vision-language encoders with improved semantic understanding, localization, and dense features. *arXiv preprint arXiv:2502.14786*, 2025. 2

[80] Dmitry Ulyanov, Andrea Vedaldi, and Victor Lempitsky. Deep image prior. In *Proceedings of the IEEE conference on computer vision and pattern recognition*, pages 9446–9454, 2018. 1, 4

[81] van A Van der Schaaf and JH van van Hateren. Modelling the power spectra of natural images: statistics and information. *Vision research*, 36(17):2759–2770, 1996. 1

[82] Singanallur V Venkatakrishnan, Charles A Bouman, and Brendt Wohlberg. Plug-and-play priors for model based reconstruction. In *2013 IEEE global conference on signal and information processing*, pages 945–948. IEEE, 2013. 1, 6

[83] Jianyi Wang, Zongsheng Yue, Shangchen Zhou, Kelvin CK Chan, and Chen Change Loy. Exploiting diffusion prior for real-world image super-resolution. *International Journal of Computer Vision*, 132(12):5929–5949, 2024. 6, 9, 10, 11

[84] Runze Wang, Zeli Chen, Zhiyun Song, Wei Fang, Jiajin Zhang, Danyang Tu, Yuxing Tang, Minfeng Xu, Xianghua Ye, Le Lu, et al. Anatomy-aware low-dose ct denoising via pretrained vision models and semantic-guided contrastive learning. In *International Conference on Medical Image Computing and Computer-Assisted Intervention*, pages 13–23. Springer, 2025. 1

[85] Ruiyi Wang, Yushuo Zheng, Zicheng Zhang, Chunyi Li, Shuaicheng Liu, Guangtao Zhai, and Xiaohong Liu. Learning hazing to dehazing: Towards realistic haze generation for real-world image dehazing. In *Proceedings of the Computer Vision and Pattern Recognition Conference*, pages 23091–23100, 2025. 1

[86] Sen Wang, Shao Zeng, Tianjun Gu, Zhizhong Zhang, Ruixin Zhang, Shouhong Ding, Jingyun Zhang, Jun Wang, Xin Tan, Yuan Xie, et al. From enhancement to understanding: Build a generalized bridge for low-light vision via semantically consistent unsupervised fine-tuning. In *Proceedings of the IEEE/CVF International Conference on Computer Vision*, pages 13804–13814, 2025. 1

[87] Tao Wang, Peiwen Xia, Bo Li, Peng-Tao Jiang, Zhe Kong, Kaihao Zhang, Tong Lu, and Wenhan Luo. Moerl: When mixture-of-experts meet reinforcement learning for adverse weather image restoration. In *Proceedings of the IEEE/CVF International Conference on Computer Vision*, pages 13673–13683, 2025. 1

[88] Xintao Wang, Liangbin Xie, Chao Dong, and Ying Shan. Real-esrgan: Training real-world blind super-resolution with pure synthetic data. In *Proceedings of the IEEE/CVF international conference on computer vision*, pages 1905–1914, 2021. 5

[89] Xinlong Wang, Xiaosong Zhang, Zhengxiong Luo, Quan Sun, Yufeng Cui, Jinsheng Wang, Fan Zhang, Yueze Wang, Zhen Li, Qiying Yu, et al. Emu3: Next-token prediction is all you need. *arXiv preprint arXiv:2409.18869*, 2024. 3, 5, 7

[90] Yongzhen Wang, Yongjun Li, Zhuoran Zheng, Xiao-Ping Zhang, and Mingqiang Wei. M2restore: Mixture-of-experts-based mamba-cnn fusion framework for all-in-one image restoration. *arXiv preprint arXiv:2506.07814*, 2025. 2

[91] Chen Wei, Wenjing Wang, Wenhan Yang, and Jiaying Liu. Deep retinex decomposition for low-light enhancement. *arXiv preprint arXiv:1808.04560*, 2018. 6

[92] Hongyang Wei, Shuaizheng Liu, Chun Yuan, and Lei Zhang. Perceive, understand and restore: Real-world image super-resolution with autoregressive multimodal generative models. *arXiv preprint arXiv:2503.11073*, 2025. 5, 6, 7, 9, 10, 11

[93] Pengxu Wei, Ziwei Xie, Hannan Lu, Zongyuan Zhan, Qixiang Ye, Wangmeng Zuo, and Liang Lin. Component divide-and-conquer for real-world image super-resolution. In *European conference on computer vision*, pages 101–117. Springer, 2020. 6

[94] Andrew P Witkin. Scale-space filtering. In *Readings in computer vision*, pages 329–332. Elsevier, 1987. 1

[95] Chengyue Wu, Xiaokang Chen, Zhiyu Wu, Yiyang Ma, Xingchao Liu, Zizheng Pan, Wen Liu, Zhenda Xie, Xingkai Yu, Chong Ruan, et al. Janus: Decoupling visual encoding for unified multimodal understanding and generation. In *Proceedings of the Computer Vision and Pattern Recognition Conference*, pages 12966–12977, 2025. 2, 3, 5

[96] Gang Wu, Junjun Jiang, Yijun Wang, Kui Jiang, and Xianming Liu. Debiased all-in-one image restoration with task uncertainty regularization. In *Proceedings of the AAAI Conference on Artificial Intelligence*, pages 8386–8394, 2025. 1

[97] Rongyuan Wu, Lingchen Sun, Zhiyuan Ma, and Lei Zhang. One-step effective diffusion network for real-world image super-resolution. *Advances in Neural Information Processing Systems*, 37:92529–92553, 2024. 5, 6, 9, 10, 11

[98] Rongyuan Wu, Tao Yang, Lingchen Sun, Zhengqiang Zhang, Shuai Li, and Lei Zhang. Seesr: Towards semantics-aware real-world image super-resolution. In *Proceedings of the IEEE/CVF conference on computer vision and pattern recognition*, pages 25456–25467, 2024. 5, 6, 9, 10, 11

[99] Jinheng Xie, Weijia Mao, Zechen Bai, David Junhao Zhang, Weihao Wang, Kevin Qinghong Lin, Yuchao Gu, Zhijie Chen, Zhenheng Yang, and Mike Zheng Shou.

Show-o: One single transformer to unify multimodal understanding and generation. *arXiv preprint arXiv:2408.12528*, 2024. 2

[100] Xinxin Xie, Qing Zhang, and Wei-Shi Zheng. Diffusion-based event generation for high-quality image deblurring. In *Proceedings of the Computer Vision and Pattern Recognition Conference*, pages 2194–2203, 2025. 1

[101] Shuning Xu, Binbin Song, Xiangyu Chen, Xina Liu, and Jiantao Zhou. Image demoiréing in raw and srgb domains. In *European Conference on Computer Vision*, pages 108–124. Springer, 2024. 1

[102] Ling Yang, Ye Tian, Bowen Li, Xincheng Zhang, Ke Shen, Yunhai Tong, and Mengdi Wang. Mmada: Multimodal large diffusion language models. *arXiv preprint arXiv:2505.15809*, 2025. 2, 3

[103] Tao Yang, Rongyuan Wu, Peiran Ren, Xuansong Xie, and Lei Zhang. Pixel-aware stable diffusion for realistic image super-resolution and personalized stylization. In *European conference on computer vision*, pages 74–91. Springer, 2024. 6, 9, 10, 11

[104] Wenhan Yang, Robby T Tan, Jiashi Feng, Zongming Guo, Shuicheng Yan, and Jiaying Liu. Joint rain detection and removal from a single image with contextualized deep networks. *IEEE transactions on pattern analysis and machine intelligence*, 42(6):1377–1393, 2019. 5, 6

[105] Wenhan Yang, Wenjing Wang, Haofeng Huang, Shiqi Wang, and Jiaying Liu. Sparse gradient regularized deep retinex network for robust low-light image enhancement. *IEEE Transactions on Image Processing*, 30:2072–2086, 2021. 5, 6

[106] Tian Ye, Sixiang Chen, Wenhao Chai, Zhaohu Xing, Jing Qin, Ge Lin, and Lei Zhu. Learning diffusion texture priors for image restoration. In *Proceedings of the IEEE/CVF conference on computer vision and pattern recognition*, pages 2524–2534, 2024. 1

[107] Xunpeng Yi, Han Xu, Hao Zhang, Linfeng Tang, and Jiayi Ma. Diff-retinex: Rethinking low-light image enhancement with a generative diffusion model. In *Proceedings of the IEEE/CVF international conference on computer vision*, pages 12302–12311, 2023. 1

[108] Runpeng Yu, Xinyin Ma, and Xinchao Wang. Dimple: Discrete diffusion multimodal large language model with parallel decoding. *arXiv preprint arXiv:2505.16990*, 2025. 3

[109] Eduard Zamfir, Zongwei Wu, Nancy Mehta, Yuedong Tan, Danda Pani Paudel, Yulun Zhang, and Radu Timofte. Complexity experts are task-discriminative learners for any image restoration. In *Proceedings of the Computer Vision and Pattern Recognition Conference*, pages 12753–12763, 2025. 2, 6, 9, 10, 11

[110] Cheng Zhang, Yu Zhu, Qingsen Yan, Jinqiu Sun, and Yan-ning Zhang. All-in-one multi-degradation image restoration network via hierarchical degradation representation. In *Proceedings of the 31st ACM international conference on multimedia*, pages 2285–2293, 2023. 2

[111] H Zhang, Z Duan, X Wang, Y Zhao, W Lu, Z Di, Y Xu, Y Chen, and Y Zhang. Nexus-gen: Unified image understanding, generation, and editing via pre-filled autoregression in shared embedding space. *arXiv preprint arXiv:2504.21356*, 2025. 7, 12

[112] Kai Zhang, Wangmeng Zuo, Yunjin Chen, Deyu Meng, and Lei Zhang. Beyond a gaussian denoiser: Residual learning of deep cnn for image denoising. *IEEE transactions on image processing*, 26(7):3142–3155, 2017. 1

[113] Dian Zheng, Xiao-Ming Wu, Shuzhou Yang, Jian Zhang, Jian-Fang Hu, and Wei-Shi Zheng. Selective hourglass mapping for universal image restoration based on diffusion model. In *Proceedings of the IEEE/CVF conference on computer vision and pattern recognition*, pages 25445–25455, 2024. 2

[114] Mo Zhou, Keren Ye, Mauricio Delbracio, Peyman Milanfar, Vishal M Patel, and Hossein Talebi. Unires: Universal image restoration for complex degradations. *arXiv preprint arXiv:2506.05599*, 2025. 1, 2

[115] Tianwen Zhou, Jing Wang, Songtao Wu, and Kuanhong Xu. Prodehaze: Prompting diffusion models toward faithful image dehazing. *arXiv preprint arXiv:2503.17488*, 2025. 1

FAPE-IR: Frequency-Aware Planning and Execution Framework for All-in-One Image Restoration

Supplementary Material

6. Distortions and Over-Generation in AR/FM and Adversarial Training for Low-Level Restoration

6.1. Notation and Standing Assumptions

Let $\mathcal{X} = \mathbb{R}^d$ denote image space with Fourier variable $\omega \in \mathbb{R}^d$. Let $p \equiv p_{\text{data}}$ be the ground-truth image law and q_θ the model law of generator G_θ . For a smoothing schedule $\sigma_t \geq 0$, define $p_t := p * \mathcal{N}(0, \sigma_t^2 I)$ and write \hat{f} for the Fourier transform. Let $\Phi : \mathcal{X} \rightarrow \mathbb{R}^m$ be a fixed perceptual map (LPIPS), frozen during training. Expectations are finite.

We consider a standard linear degradation model for low-level restoration:

$$c = Hx + \eta, \quad x \sim p, \quad \eta \sim \mathcal{N}(0, \sigma_\eta^2 I), \quad (6)$$

with known operator $H : \mathcal{X} \rightarrow \mathcal{X}$ (e.g., blur+downsample for SR, convolutional blur for deblurring, masking for inpainting). Denote the conditional posterior by $p(x | c)$ and its smoothed versions $p_t(x | c) := p(\cdot | c) * \mathcal{N}(0, \sigma_t^2 I)$.

Assumption 1 (Spectral regularity of natural images). *The power spectrum of natural images satisfies:*

$$S_{xx}(\omega) := \mathbb{E}|\hat{x}(\omega)|^2 \asymp \|\omega\|^{-\kappa}, \quad \kappa > 0, \quad (7)$$

so that energy is mainly concentrated at low frequencies and decays polynomially with frequency [81]. This reflects the empirical smoothness of natural images and excludes degenerate high-frequency dominated signals [6, 19, 24, 67, 69, 81].

Assumption 2 (Forward operator). *H is linear, bounded, and shift-invariant on the domain of interest with frequency response $\hat{H}(\omega)$. For blur/downsample/inpainting, $|\hat{H}(\omega)|$ decays (or vanishes) for large $\|\omega\|$ or outside the passband [29, 32, 80].*

Assumption 3 (Regularized flow path). *The conditional path is given by Gaussian smoothing [43, 71, 94]:*

$$p_t(\cdot | c) = p(\cdot | c) * K_{\sigma_t}, \quad (8)$$

with σ_t smooth in t . Then p_t is C^1 in t , and there exists a drift $v_t^*(\cdot | c)$ such that $\partial_t p_t + \nabla \cdot (v_t^* p_t) = 0$. For $p_t = p * \mathcal{N}(0, \sigma_t^2 I)$ one can take the explicit choice [65, 82]:

$$v_t^*(x, c) = -\frac{\sigma_t^2}{2} \nabla \log p_t(x | c). \quad (9)$$

Assumption 4 (Lipschitz drift and locally bounded conditional density). *Each $v_t^*(\cdot | c)$ is L -Lipschitz. Moreover, for each t there exists a compact set $K_t \subset \mathcal{X}$ such that the conditional densities are locally bounded and bounded away from zero on K_t :*

$$0 < m_t \leq p_t(x | c) \leq M_t < \infty \quad \text{for all } x \in K_t, \quad (10)$$

uniformly (in the sense appropriate to the expectations we consider). All expectations in this paper are taken over x restricted to K_t (or via truncation/limit arguments), which is natural in low-level restoration where reconstructions lie in a plausible compact region.

Assumption 5 (IPM critic: attainment and compact parameterization). *We assume $d_{\mathcal{F}}(p, q) = \sup_{f \in \mathcal{F}} (\mathbb{E}_p f - \mathbb{E}_q f)$ with $\mathcal{F} = \{f_\psi : \psi \in \Psi\}$ parameterized by a compact set Ψ , such that the supremum is attained at some $\psi^* \in \Psi$. Then Danskin's theorem applies to yield:*

$$\nabla_\theta d_{\mathcal{F}}(p, q_\theta) = -\mathbb{E}[J_{G_\theta}^\top \nabla_x f_{\psi^*}(G_\theta)]. \quad (11)$$

(Alternatively, one may work with subgradients if \mathcal{F} is non-compact, e.g. the 1-Lipschitz ball for W_1 .) See [2, 3, 72].

6.2. Objectives (Restoration Setting)

Autoregression (AR). Conditioned on c , the chain factorization is $q_\theta(x | c) = \prod_{t=1}^T q_\theta(x_t | x_{<t}, c)$, and

$$\theta_{\text{AR}}^* \in \arg \min_{\theta} \mathbb{E}_{c \sim p(c)} \text{KL}(p(\cdot | c) \| q_\theta(\cdot | c)). \quad (12)$$

Flow Matching (FM). FM is a general framework for distribution transport, with Rectified Flow as the linear-path special case; related score-based views connect to diffusion/SDE modeling and score matching [23, 45, 46, 70]. Here we adopt the basic form based on conditional scores of smoothed posteriors:

$$\theta_{\text{FM}}^* \in \arg \min_{\theta} \int_0^1 w(t) \mathbb{E}_{c \sim p(c)} \mathbb{E}_{x_t \sim p_t(\cdot | c)} \|s_\theta(x_t, c, t) - \nabla \log p_t(x_t | c)\|_2^2 dt. \quad (13)$$

Adversarial Training. Given pairs (c, x) , augment the composite objective with a measurement term:

$$\begin{aligned} \mathcal{J}(\theta) = & \lambda d_{\mathcal{F}}(p, q_\theta) + \alpha \mathbb{E} \|G_\theta(c) - x\|_2^2 \\ & + \beta \mathbb{E} \|\Phi(G_\theta(c)) - \Phi(x)\|_2^2, \quad \lambda, \alpha, \beta \geq 0, \end{aligned} \quad (14)$$

with $d_{\mathcal{F}}$ often chosen as W_1 (WGAN) [2, 3, 72].

6.3. AR Causes Artifacts and Over-Generation

Modeling assumptions for AR proofs. We make explicit the family of admissible AR conditionals and the inference rule used at test time.

Assumption 6 (Single-mode AR conditionals or deterministic limit). *For each t , conditionals $q_\theta(x_t | x_{<t}, c)$ belong to a centered, symmetric, log-concave location family:*

$$\mathcal{Q} := \{x_t \mapsto f_\sigma(x_t - \mu_t) : \mu_t \in \mathbb{R}^{d_t}, \sigma \in (0, \sigma_{\max}]\}, \quad (15)$$

where f_σ is even, strictly log-concave, smooth in σ , and the deterministic limit $\sigma \rightarrow 0$, i.e. $q_\theta(\cdot | x_{<t}, c) \Rightarrow \delta_{\mu_t(x_{<t}, c)}$.

Assumption 7 (Greedy or vanishing-temperature decoding). *At test time, decoding is either greedy ($x_t = \arg \max q_\theta(\cdot | x_{<t}, c)$) or stochastic with temperature $\tau \downarrow 0$ so that $x_t \Rightarrow \arg \max q_\theta(\cdot | x_{<t}, c)$ in probability.*

Definition 1 (Posterior $\ker(H)$ -ambiguity at step t). *Let $E_t : \mathbb{R}^{d_t} \rightarrow \mathcal{X}$ be the (fixed) embedding that maps the local step- t variable into image space. We say that the step- t posterior exhibits a symmetric $\ker(H)$ -ambiguity with gap $u_t \in \mathbb{R}^{d_t}$ if for a measurable set $A_t \subseteq \{(x_{<t}, c)\}$ with $p(A_t) \geq \rho_t > 0$,*

$$\begin{aligned} p(x_t | x_{<t}, c) &= \frac{1}{2} \delta_{x_t^{(0)}(x_{<t}, c) + u_t} \\ &\quad + \frac{1}{2} \delta_{x_t^{(0)}(x_{<t}, c) - u_t}, \quad (16) \\ H E_t u_t &= 0. \end{aligned}$$

Here $x_t^{(0)}$ is the posterior midpoint in the local coordinates; the corresponding image-space ambiguity direction is $E_t u_t$.

Theorem 1 (AR deterministic collapse along $\ker(H)$). *Under Assumptions 6–7 and Definition 1, the maximum-likelihood solution of Equation 12 satisfies*

$$\mu_t^*(x_{<t}, c) = x_t^{(0)}(x_{<t}, c) \text{ for } p\text{-a.e. } (x_{<t}, c) \in A_t, \quad (17)$$

and the decoded token obeys $x_t = \mu_t^*(x_{<t}, c)$ a.s. in the greedy limit. Consequently, the image-space component of x_t along the ambiguity direction $\text{span}\{E_t u_t\}$ is collapsed to zero mean, removing genuine $\pm E_t u_t$ variability and inducing structured artifacts aligned with $\ker(H)$.

Proof. Fix $(x_{<t}, c) \in A_t$. By Assumption 6 the conditional log-likelihood for center μ is $\ell(\mu) = \log f_\sigma(x_t^{(0)} + u_t - \mu) + \log f_\sigma(x_t^{(0)} - u_t - \mu)$. Since f_σ is even and strictly log-concave, ℓ is strictly concave and achieves its unique maximum at the midpoint $\mu = x_t^{(0)}$. Teacher forcing MLE therefore yields $\mu_t^* = x_t^{(0)}$ on A_t , and by Assumption 7 the decoded value equals μ_t^* almost surely in the deterministic limit. Because $H E_t u_t = 0$, the collapsed direction is exactly unobservable in c , hence constitutes artifact-prone freedom. \square

Remark 1 (When collapse can be avoided). If the conditional family admits *explicit multimodality* (e.g. mixture components with separate centers and nontrivial sampling at test time), Theorem 1 need not hold. This motivates latent-variable AR or distributional heads when H is severely rank-deficient.

From local collapse to global artifact patterns. We connect stepwise ambiguity to image-level artifacts via an additive geometric functional.

Definition 2 (Artifact deficit). *Let $\Pi : \mathcal{X} \rightarrow \mathbb{R}_{\geq 0}$ be a convex seminorm measuring nullspace-structured deviations (e.g. $\Pi(x) = \|P_{\ker(H)}x\|_2$ or a high-pass seminorm restricted to $\ker(H)$). For a sample $\tilde{x} \sim q_\theta(\cdot | c)$ define the artifact deficit:*

$$\mathcal{D}(\tilde{x}; c) := \mathbb{E}_{p(x|c)} \Pi(x) - \Pi(\tilde{x}). \quad (18)$$

By Jensen's inequality and Theorem 1, when the posterior on a direction is symmetric and decoding collapses to the midpoint, \mathcal{D} is typically nonnegative; its positivity quantifies the loss of genuine posterior variability along $\ker(H)$.

Proposition 1 (TV-based upper bound on deficit over ambiguity sets). *Suppose Definition 1 holds for indices $t \in \mathcal{T} \subseteq \{1, \dots, T\}$ with probabilities $\{\rho_t\}$ and ambiguity vectors $\{u_t\}$. Let Π be any convex seminorm that is strictly convex on $\ker(H)$. For each $R > 0$, define the truncated seminorm $\Pi_R := \min\{\Pi, R\}$ to ensure boundedness on K_t (Assumption 4). Define on A_t :*

$$\bar{\varepsilon}_t^{(A)} := \underset{(x_{<t}, c) \in A_t}{\text{ess sup}} \text{TV}(p(\cdot | x_{<t}, c), q_\theta(\cdot | x_{<t}, c)). \quad (19)$$

Let

$$\begin{aligned} \Delta_{\Pi_R}^{\max} &:= \sup_{t \leq T} \sup_{(x_{<t}, c) \in A_t} \frac{1}{2} \left(\Pi_R(x_t^{(0)} + u_t) \right. \\ &\quad \left. + \Pi_R(x_t^{(0)} - u_t) - 2\Pi_R(x_t^{(0)}) \right). \end{aligned} \quad (20)$$

Then

$$\begin{aligned} \mathbb{E}[\mathcal{D}_R(\tilde{x}; c)] &\leq \Delta_{\Pi_R}^{\max} \sum_{t=1}^T \rho_t \bar{\varepsilon}_t^{(A)} \\ &\quad + \mathbb{E}[\mathcal{D}_R(\tilde{x}; c) \mathbf{1}_{(\cup_t A_t)^c}], \end{aligned} \quad (21)$$

where \mathcal{D}_R is defined by replacing Π with Π_R in Definition 2. Passing to the limit $R \rightarrow \infty$ by monotone convergence yields the same bound for \mathcal{D} provided the moments in Assumption 4 hold. The complement term can be further bounded once additional structure outside $\cup_t A_t$ is specified (e.g. no nullspace ambiguity or separate curvature bounds).

Proof. On each A_t , for bounded Π_R we have $|\mathbb{E}_p \Pi_R - \mathbb{E}_q \Pi_R| \leq \|\Pi_R\|_\infty \text{TV}(p, q)$. Summing over $t \in \mathcal{T}$ and using the definition of $\Delta_{\Pi_R}^{\max}$ yields Equation 21. The monotone limit follows by Assumption 4. \square

Quantifying Exposure Amplification in Rollout.

Assumption 8 (Lipschitz artifact seminorm). *There exists $L_\Pi > 0$ such that $|\Pi(x) - \Pi(y)| \leq L_\Pi \|P_{\ker(H)}(x - y)\|_2$ for all x, y . When needed, we also use the truncated seminorm $\Pi_R := \min\{\Pi, R\}$ to guarantee integrability; all bounds pass to the limit $R \rightarrow \infty$ by monotone convergence under our moment assumptions.*

Proposition 2 (Positive artifact deficit under repeated ambiguity). *Suppose Definition 1 holds for indices $t \in \mathcal{T} \subseteq \{1, \dots, T\}$ with probabilities $\{\rho_t\}$ and ambiguity vectors $\{u_t\}$. Let Π be any convex seminorm that is strictly convex on $\ker(H)$. Then:*

$$\begin{aligned} \mathbb{E}[\mathcal{D}(\tilde{x}; c)] &\geq \sum_{t \in \mathcal{T}} \rho_t \left[\frac{1}{2} \Pi(x_t^{(0)} + u_t) \right. \\ &\quad \left. + \frac{1}{2} \Pi(x_t^{(0)} - u_t) \right] - \sum_{t \in \mathcal{T}} \rho_t \Pi(x_t^{(0)}). \end{aligned} \quad (22)$$

Proof. Fix $(x_{<t}, c) \in A_t$. Under p , Π sees two symmetric values around $x_t^{(0)}$; by convexity $\frac{1}{2} \Pi(x_t^{(0)} + u_t) + \frac{1}{2} \Pi(x_t^{(0)} - u_t) \geq \Pi(x_t^{(0)})$, with strict inequality by strict convexity if $u_t \neq 0$. Under q_θ , Theorem 1 yields the degenerate value $\Pi(x_t^{(0)})$. Taking differences and averaging over A_t gives the bound; summing over indices $t \in \mathcal{T}$ yields the stated inequality. A matching lower/upper bound in general needs additional independence/orthogonality assumptions and is omitted here. \square

Exposure bias and accumulation. During training, loss is minimized with teacher forcing; at test time the model uses its own predictions. Define the per-step deviation:

$$\begin{aligned} \delta_t(x_{<t}, c) &:= \text{TV}(p(\cdot | x_{<t}, c), q_\theta(\cdot | x_{<t}, c)), \\ \varepsilon_t &:= \mathbb{E}_{x_{<t} \sim p(\cdot | c)} \delta_t(x_{<t}, c). \end{aligned} \quad (23)$$

We also write the *worst-case* per-step deviation $\bar{\varepsilon}_t := \text{ess sup}_{x_{<t}, c} \delta_t(x_{<t}, c)$.

Lemma 1 (Accumulation of local deviations). *For the AR factorizations of p and q_θ using consistent measurable versions of the conditionals, the following bounds hold:*

$$\text{TV}(p(\cdot | c), q_\theta(\cdot | c)) \leq 1 - \prod_{t=1}^T (1 - \bar{\varepsilon}_t) \leq \sum_{t=1}^T \bar{\varepsilon}_t, \quad (24)$$

and, independently,

$$\text{TV}(p(\cdot | c), q_\theta(\cdot | c)) \leq \sum_{t=1}^T \varepsilon_t. \quad (25)$$

In particular, for small $\{\alpha_t\}$ with $\alpha_t \in \{\bar{\varepsilon}_t\}$,

$$1 - \prod_{t=1}^T (1 - \alpha_t) = \sum_{t=1}^T \alpha_t + \mathcal{O}\left(\sum_{s < t} \alpha_s \alpha_t\right). \quad (26)$$

Chain rule and conditional optimization. By standard decomposition,

$$\begin{aligned} \text{KL}(p(\cdot | c) \| q_\theta(\cdot | c)) &= \sum_{t=1}^T \mathbb{E}_{x \sim p(\cdot | c)} \\ &\quad \left[\text{KL}(p(\cdot | x_{<t}, c) \| q_\theta(\cdot | x_{<t}, c)) \right]. \end{aligned} \quad (27)$$

Thus training matches each conditional distribution separately. However, if $p(x_t | x_{<t}, c)$ admits multiple plausible continuations (e.g. along weakly observed directions of H), then any surrogate that collapses to a single conditional predictor necessarily *destroys* these alternatives. This mismatch does not show up as blur in practice, samples remain sharp, but it manifests as systematic artifacts where the model enforces spurious “averaged” structures.

Proof of Equation 27. Write $p(x | c) = \prod_{t=1}^T p(x_t | x_{<t}, c)$ and $q_\theta(x | c) = \prod_{t=1}^T q_\theta(x_t | x_{<t}, c)$. Then

$$\begin{aligned} \text{KL}(p \| q_\theta) &= \mathbb{E}_{x \sim p} \left[\sum_{t=1}^T \log \frac{p(x_t | x_{<t}, c)}{q_\theta(x_t | x_{<t}, c)} \right] \\ &= \sum_{t=1}^T \mathbb{E}_{x_{<t} \sim p} \text{KL}(p(\cdot | x_{<t}, c) \| q_\theta(\cdot | x_{<t}, c)). \end{aligned} \quad (28)$$

Hence Equation 27 holds, formalizing that AR training aligns each conditional factor separately. \square

Proposition 3 (Nullspace ambiguity induces artificial averaging). *Let H in Equation 6 have nontrivial nullspace and suppose the posterior $p(x | c)$ assigns equal mass to $x_\pm = x_0 \pm u$ with $Hu = 0$. Then the Bayes point estimator is:*

$$\hat{x} = \mathbb{E}[x | c] = x_0, \quad (29)$$

which cancels the true variability $\pm u$. Thus any deterministic AR predictor removes detail along u , creating structured artifacts not present in the true posterior (while stochastic decoding that breaks symmetry may inconsistently realize one of the modes).

Proof. Under squared loss, the Bayes estimator equals the conditional mean:

$$\hat{x} = \mathbb{E}[x | c] = \frac{1}{2}(x_0 + u) + \frac{1}{2}(x_0 - u) = x_0. \quad (30)$$

Hence the genuine posterior variability $\pm u$ (unobservable since $Hu = 0$) is averaged out.

Moreover, consider an AR conditional family restricted to a symmetric log-concave location family (e.g. $x_t \sim \mathcal{N}(\mu_t, \sigma^2 I)$ with fixed σ , or the $\sigma \rightarrow 0$ deterministic limit). Given a symmetric two-point posterior $\frac{1}{2}\delta_{x_0+u} + \frac{1}{2}\delta_{x_0-u}$, the conditional MLE for the center is the midpoint x_0 by symmetry and concavity: the log-likelihood takes the form

$\ell(\mu) = \log f(x_0 + u - \mu) + \log f(x_0 - u - \mu)$ with f log-concave and even; ℓ is concave and maximized at $\mu = x_0$ (where the two arguments are opposite), yielding the same collapse to x_0 . Thus single-mode/deterministic conditionals enforce artificial averaging along nullspace directions. \square

Takeaways. AR provably enforces *deterministic resolutions* of measurement ambiguities, averages away legitimate alternatives along nullspace directions, and accumulates local deviations into global structural errors. Unlike blur, which is not observed in practice, these mechanisms explain the clear yet artifact-laden outputs: geometric kinks, inconsistent fills, and over-generation of non-existent structures. Exposure/rollout issues are closely related to scheduled sampling, sequence-level training, and imitation-learning reductions [5, 62, 66].

Remark on bounds. The product-form term in Equation 24 uses worst-case per-step deviations $\bar{\varepsilon}_t$ and is tight for sequential maximal couplings [80]. A nontrivial *lower* bound on $\text{TV}(p, q_\theta)$ or on artifact deficits in terms of per-step quantities generally requires additional independence/de-coupling assumptions; without them we provide only the robust upper bounds above (cf. Proposition 1).

6.4. Why Distortions and Over-generation Appear in Flow Matching Optimization

A precise local sandwich. We refine the conditional spectral sandwich (Theorem 3, stated later) by (i) focusing on the small-perturbation regime and (ii) replacing $|\widehat{H}(\omega)|^2$ with an *information transfer coefficient* $\Xi_t(\omega)$ capturing the H -noise-prior interplay [80].

Assumption 9 (Small-perturbation regime and bounded densities). *Let $p_t(\cdot | c) = p(\cdot | c) * K_{\sigma_t}$ and assume that $q_{\theta,t}(\cdot | c)$ admits the representation:*

$$q_{\theta,t}(\cdot | c) = q_\theta(\cdot | c) * K_{\sigma_t}, \quad p_t(\cdot | c) = p(\cdot | c) * K_{\sigma_t}. \quad (31)$$

Define the unsmoothed discrepancy $\delta(\cdot | c) := q_\theta(\cdot | c) - p(\cdot | c)$ and its smoothed version

$$\Delta_t(\cdot | c) := \delta(\cdot | c) * K_{\sigma_t}, \quad (32)$$

so that $q_{\theta,t} = p_t + \Delta_t$ and $\int \Delta_t(x | c) dx = 0$. Assume $\|\Delta_t\|_{L^\infty} \leq \eta_t m_t / 2$ with some $0 < \eta_t < 1$ and $\|\nabla \Delta_t\|_{L^2} < \infty$, where $0 < m_t \leq p_t \leq M_t < \infty$ are as in Assumption 4.

Definition 3 (Information transfer coefficient). *In the linear-Gaussian setting with $x \sim \mathcal{N}(0, S_{xx})$ and $c = Hx + \eta$, define the frequency-wise posterior information weight*

$$\Xi_{\text{LG}}(\omega) := \frac{|\widehat{H}(\omega)|^2}{\sigma_\eta^2 + |\widehat{H}(\omega)|^2 S_{xx}(\omega)} \in [0, 1/\sigma_\eta^2] \quad (33)$$

which vanishes where $\widehat{H}(\omega) = 0$ and increases with the local posterior SNR. In the general small-perturbation regime of Assumption 9, there exist constants $0 < c_t^{(1)} \leq c_t^{(2)} < \infty$ (depending only on (m_t, M_t) and low-order moments of $p_t(\cdot | c)$, but not on ω) such that:

$$c_t^{(1)} \Xi_{\text{LG}}(\omega) \leq \Xi_t(\omega) \leq c_t^{(2)} \Xi_{\text{LG}}(\omega). \quad (34)$$

Lemma 2 (Pythagorean decomposition in $L^2(p_t)$). *Let $s_\theta = \nabla \log q_{\theta,t} + r_{\theta,t}$ with $r_{\theta,t} \in L^2(p_t)$. Then*

$$\begin{aligned} \mathbb{E}_{p_t} \|s_\theta - \nabla \log p_t\|_2^2 &= D_F(p_t \| q_{\theta,t}) + \|r_{\theta,t}\|_{L^2(p_t)}^2 \\ &\quad + 2 \langle r_{\theta,t}, \nabla \log q_{\theta,t} - \nabla \log p_t \rangle_{L^2(p_t)}. \end{aligned} \quad (35)$$

If $r_{\theta,t}$ is the $L^2(p_t)$ -orthogonal residual of projecting $\nabla \log p_t$ onto the model class, the cross term vanishes and the training loss splits into a Fisher part plus an approximation error (this orthogonality is an idealized projection property and need not hold for general parameterizations).

Theorem 2 (Local Fisher sandwich with spectral weights). *Under Assumptions 2, 4, and 9, there exist finite constants $0 < c_t \leq C_t < \infty$ such that the (conditional) Fisher divergence satisfies:*

$$\begin{aligned} &\int_0^1 w(t) c_t \int_{\mathbb{R}^d} \underbrace{\|\omega\|^2 e^{-\sigma_t^2 \|\omega\|^2} \Xi_t(\omega)}_{=: \widetilde{W}_t(\omega)} \mathbb{E}_c |\widehat{\delta}(\omega | c)|^2 d\omega dt \\ &\leq \int_0^1 w(t) D_F(p_t(\cdot | c) \| q_{\theta,t}(\cdot | c)) dt \\ &\leq \int_0^1 w(t) C_t \int_{\mathbb{R}^d} \widetilde{W}_t(\omega) \mathbb{E}_c |\widehat{\delta}(\omega | c)|^2 d\omega dt + R, \end{aligned} \quad (36)$$

with a quadratic remainder $0 \leq R \leq \int_0^1 w(t) \kappa_t \|\Delta_t\|_{L^\infty}^2 dt$, where κ_t depends on (m_t, M_t) and the Lipschitz constants in Assumption 4. As $\max_t \|\Delta_t\|_{L^\infty} \rightarrow 0$, we have $R \rightarrow 0$, and Equation 36 becomes an equality up to factors c_t, C_t . Moreover, on any time window where $\sigma_t \in [\sigma_{\min}, \sigma_{\max}]$ is bounded, the constants c_t, C_t can be chosen uniformly bounded with respect to t on that window.

Corollary 1 (From Fisher to the FM objective). *Under the setting of Lemma 2, the FM loss in Equation 13 decomposes into the Fisher term bounded by Equation 36 plus a nonnegative approximation error $\|r_{\theta,t}\|_{L^2(p_t)}^2$ (when the cross term vanishes). Hence all conclusions drawn from Equation 36 for D_F transfer to \mathcal{L}_{FM} up to adding this nonnegative term.*

Corollary 2 (High-frequency underweighting and nullspace gaps). *Under Theorem 2, for any set $\Omega \subset \mathbb{R}^d$:*

1. If $\inf_{\omega \in \Omega} \|\omega\| \rightarrow \infty$, then $\sup_{\omega \in \Omega} \widetilde{W}_t(\omega) \rightarrow 0$ exponentially in $\|\omega\|$, hence discrepancies concentrated in Ω contribute arbitrarily little to \mathcal{L}_{FM} .

2. If $|\widehat{H}(\omega)| = 0$ on Ω , then $\Xi_t(\omega) = 0$ on Ω (for the linear-Gaussian definition) and thus $\widetilde{W}_t(\omega) = 0$; this establishes exact blindness on $\ker(H)$ bands. When $|\widehat{H}(\omega)|$ is nonzero but very small, the weight remains near-blind.

Early-time forgetting bound.

Proposition 4 (Quantified forgetting under strong smoothing (expectation version)). *Let $p_t(\cdot | c) = p(\cdot | c) * \mathcal{N}(0, \sigma_t^2 I)$ and assume $\mathbb{E}\|Hx\| < \infty$. Then there exists a constant $C_d > 0$ depending only on the dimension such that:*

$$\begin{aligned} \mathbb{E}_c \text{TV}(p_t(\cdot | c), p(\cdot)) &\leq C_d \times \\ \min \left\{ 1, \frac{1}{\sigma_t} \mathbb{E}_c W_1(p(\cdot | c), p(\cdot)) \right\} &\xrightarrow{\sigma_t \rightarrow \infty} 0. \end{aligned} \quad (37)$$

Proof sketch. Convolution with K_{σ_t} smooths test functions by shrinking their effective Lipschitz seminorm by $\|\nabla K_{\sigma_t}\|_{L^1} = \Theta(1/\sigma_t)$; apply the Kantorovich–Rubinstein dual for TV/Wasserstein comparison on smoothed measures and integrate over c .

Remark 2 (Uniform version under additional boundedness). If, in addition, c is restricted to a compact set (or one assumes $\sup_c W_1(p(\cdot | c), p(\cdot)) < \infty$), then the same argument yields:

$$\begin{aligned} \sup_c \text{TV}(p_t(\cdot | c), p(\cdot)) &\leq \frac{C_d}{\sigma_t} \\ &\times \sigma_t \sup_c W_1(p(\cdot | c), p(\cdot)) \xrightarrow{\sigma_t \rightarrow \infty} 0. \end{aligned} \quad (38)$$

Large perceptual error with small FM loss.

Proposition 5 (Loss–distortion gap with quantitative construction). *Let Φ be L_Φ -Lipschitz. Fix a measurable $\Omega \subset \mathbb{R}^d$ with $\sup_{\omega \in \Omega} \widetilde{W}_t(\omega) \leq \epsilon_W$. Assume further that Φ is co-Lipschitz on Ω : there exist a seminorm Π_Ω supported on Ω and a constant $\kappa_\Omega > 0$ such that for all u with $\text{supp } \widehat{u} \subseteq \Omega$,*

$$\Pi_\Omega(u) \leq \kappa_\Omega^{-1} \|\Phi(u)\|_2. \quad (39)$$

Then there is a constant $C > 0$ (depending on $\Omega, \{w(t), \sigma_t\}$) and a perturbation family $\{\Delta_t\}_t$ with uniformly small $\|\Delta_t\|_\infty$ such that

$$\int_0^1 w(t) \int \widetilde{W}_t \mathbb{E}_c |\widehat{\delta}|^2 \leq \epsilon_W, \mathbb{E}\|\Phi(x) - \Phi(\tilde{x})\|_2^2 \geq C \kappa_\Omega^2. \quad (40)$$

Specifically, take $\widehat{\delta}(\omega | c) = a_t \mathbf{1}_\Omega(\omega) e^{i\varphi(c, \omega)}$ with phases chosen so that $\|\Delta_t\|_\infty \leq \|\widehat{\Delta}_t\|_{L^1} \leq |a_t| |\Omega|$, and scale a_t so that the weighted quadratic form equals ϵ_W . Hausdorff–Young and Plancherel give the stated controls; the co-Lipschitz property transfers spectral mass on Ω to a non-trivial feature deviation.

A weighted spectral view. Let $\Delta_t(x | c) := q_{\theta, t}(x | c) - p_t(x | c) = (q_\theta - p) * K_{\sigma_t}$ and write $\widehat{\cdot}$ for Fourier transforms in x . Define

$$\widetilde{W}_t(\omega) := \|\omega\|^2 e^{-\sigma_t^2 \|\omega\|^2} \Xi_t(\omega). \quad (41)$$

Theorem 3 (Conditional spectral sandwich under small perturbations). *Assume 2, 4, and 9. Then there exist finite constants $0 < c_t \leq C_t < \infty$ such that for all θ ,*

$$\begin{aligned} \int_0^1 w(t) c_t \int_{\mathbb{R}^d} \widetilde{W}_t(\omega) \\ \mathbb{E}_c |\widehat{\delta}(\omega | c)|^2 d\omega dt &\lesssim \mathcal{L}_{\text{FM}}(\theta) \\ \mathcal{L}_{\text{FM}}(\theta) &\lesssim \int_0^1 w(t) C_t \\ \int_{\mathbb{R}^d} \widetilde{W}_t(\omega) \mathbb{E}_c |\widehat{\delta}(\omega | c)|^2 d\omega dt + R, \end{aligned} \quad (42)$$

with $0 \leq R \leq \int_0^1 w(t) \kappa_t \|\Delta_t\|_{L^\infty}^2 dt$. Consequently:

- (High-frequency down-weighting) Since $\widetilde{W}_t(\omega) \propto \|\omega\|^2 e^{-\sigma_t^2 \|\omega\|^2}$, large- $\|\omega\|$ discrepancies contribute exponentially little to \mathcal{L}_{FM} .
- (Nullspace down-weighting) If $|\widehat{H}(\omega)| = 0$ on Ω , then $\Xi_t(\omega) = 0$ and $\widetilde{W}_t(\omega) = 0$ on Ω , establishing exact blindness on $\ker(H)$ bands.
- (Loss–distortion gap) By concentrating $\widehat{\delta}$ where \widetilde{W}_t is tiny and controlling $\|\Delta_t\|_\infty$, one can keep \mathcal{L}_{FM} small while incurring large pixel/perceptual deviations (cf. Proposition 5).

Takeaway 1 (Objective Bias): FM minimizes a spectrally reweighted discrepancy, where high frequencies and directions in the kernel of H are under-penalized. This leads to an *identifiability gap*, where visually distinct reconstructions can exhibit nearly identical FM loss values.

From objective bias to visible geometry: flow amplification. Let x follow the true conditional flow $\dot{x} = v_t^*(x, c, t)$ (Assumption 3) and \tilde{x} the learned flow $\dot{\tilde{x}} = v_\theta(\tilde{x}, c, t)$.

Lemma 3 (Conditional flow stability and geometric warp). *With $e_t = v_\theta - v_t^*$ and L the Lipschitz constant of v_t^* ,*

$$\|x(t) - \tilde{x}(t)\| \leq e^{Lt} \left(\|x(0) - \tilde{x}(0)\| + \int_0^t \|e_s(\tilde{x}, c, s)\| ds \right). \quad (43)$$

Corollary 3 (Edge bending (heuristic)). *Let $\Gamma \subset \mathcal{X}$ be a high-curvature level set (edge/contour). Suppose e_t is predominantly supported where the learned dynamics deviates around edges (a region where small phase errors matter most). Then even when $\int_0^1 \mathbb{E}\|e_t\|^2 dt$ is small under the FM weighting, the spatial displacement of Γ under $\tilde{x}(\cdot)$ can be $O(e^L)$ relative to local curvature radii, producing visible warps/kinks.*

Intuition. Because FM underweights high- ω errors (due to heat-kernel smoothing and measurement passband), the learned drift can be slightly wrong where edges live. The ODE then *integrates* these local, directionally coherent errors into macroscopic geometric distortions (Lemma 3).

Why over-generation (hallucinated detail) appears. Two complementary mechanisms follow from Theorem 3:

Proposition 6 (Nullspace over-generation under down-weighting). *Suppose there exists $\Omega \neq \emptyset$ with $|\widehat{H}(\omega)| = 0$ on Ω and the setting is linear-Gaussian so that $\Xi_t(\omega) = 0$ on Ω . If the generator class can realize perturbations supported on Ω (assumption on representational capacity within K_t), then for any $\epsilon > 0$ there is q_θ with $\mathcal{L}_{\text{FM}}(\theta) \leq \epsilon$ whose samples \tilde{x} contain arbitrarily strong components supported on Ω . Thus textures along $\ker H$ can be invented at negligible FM loss in this regime.*

Remark 3 (Scope vs. small-perturbation regime). The construction in Proposition 6 addresses the *attainable worst case* and is *not* restricted by the small- $\|\Delta_t\|_\infty$ assumption of Assumption 9. When $\|\Delta_t\|_\infty$ is explicitly constrained, the strength of over-generated $\ker H$ components is likewise bounded.

Proposition 7 (Early-time conditioning leakage). *Suppose $w(t)$ gives nontrivial mass to large σ_t (early times). Then $\widetilde{W}_t(\omega) \rightarrow 0$ for all ω as $\sigma_t \rightarrow \infty$, so the early-time portion of Equation 13 is weakly informative about c . By Proposition 4, we have $\mathbb{E}_c \text{TV}(p_t(\cdot | c), p_t(\cdot)) \rightarrow 0$ as $\sigma_t \rightarrow \infty$, hence the early-time loss is effectively unconditional in the strong-smoothing regime. The learned drift there tends toward the unconditional score, which injects prior textures that later stages cannot fully remove in underconstrained regions, contributing to over-generation.*

Summary of mechanisms for FM artifacts

- **Spectral bias** (Theorem 3(a)): high- ω penalties are tiny \Rightarrow **edge softness, texture loss**.
- **Nullspace blindness** (Theorem 3(b), Prop. 6): H unpenalized \Rightarrow **hallucinated detail** in underspecified regions.
- **Flow amplification** (Cor. 3): small drift errors near edges integrate to **geometric warps/kinks**.
- **Early-time leakage** (Prop. 7): weak conditioning at large σ_t injects prior textures \Rightarrow **over-generation** that later steps cannot reliably remove.

Design implications for FM in restoration.

1. **Spectral reweighting.** Modify the loss with a deconvolution factor to counter the spectral weight (W_t globally, or \widetilde{W}_t in the local view):

$$\begin{aligned} \tilde{\mathcal{L}} &= \int_0^1 w(t) \mathbb{E} \left\| \Lambda_t^{-1} (s_\theta - \nabla \log p_t) \right\|^2, \\ \widehat{\Lambda}_t(\omega) &\propto \|\omega\| e^{-\sigma_t^2 \|\omega\|^2/2} \sqrt{\Xi_t(\omega)}, \end{aligned} \quad (44)$$

with *clipping* to avoid noise amplification.

2. **Data consistency.** Interleave FM steps with projections onto $\{x : \|Hx - c\| \leq \tau\}$ or add a strong penalty $\gamma \|HG_\theta(c) - c\|^2$ during training/sampling to break nullspace blindness [6]; see also PnP/RED frameworks [23, 65, 70, 82].
3. **Edge-aware guidance.** Upweight loss contributions near high $\|\nabla_x \Phi(x)\|$ (perceptual edges) or blend an IPM on high-pass features to prevent geometric warps.
4. **Time weighting.** Reduce $w(t)$ for very large σ_t or use schedules that spend more capacity near well-conditioned times where c carries information.

7. Adversarial Training: High-Fidelity Control Without Over-Generation

7.1. Objective and Assumptions

Under Equation 6, let $G_\theta(c, z)$ be a generator with latent z , and let $d_{\mathcal{F}}$ be an Integral Probability Metric (IPM) induced by a compact function class \mathcal{F} (e.g., 1-Lipschitz critics for W_1) [3]. We consider the composite objective

$$\begin{aligned} \mathcal{J}(\theta) &= \lambda d_{\mathcal{F}}(p, q_\theta) + \alpha \mathbb{E} \|G_\theta(c, z) - x\|_2^2 \\ &\quad + \beta \mathbb{E} \|\Phi(G_\theta(c, z)) - \Phi(x)\|_2^2, \end{aligned} \quad (45)$$

with nonnegative weights λ, α, β . Here q_θ is the model law from G_θ , and $\Phi : \mathcal{X} \rightarrow \mathbb{R}^m$ is a fixed perceptual map.

Assumption 10 (Regularity). *\mathcal{F} is compact and satisfies Danskin differentiability (Assumption 5); Φ is L_Φ -Lipschitz when relating to high-frequency seminorms; G_θ is differentiable with bounded Jacobian J_{G_θ} on the support of interest; expectations are finite.*

7.2. Gradient Representation and Stationarity

Lemma 4 (IPM gradient/subgradient for the critic). *Assume $\mathcal{F} = \{f_\psi : \psi \in \Psi\}$ is a compact, parameterized class (e.g., spectrally-normalized networks) and the supremum is attained at some ψ^* . Then*

$$\nabla_\theta d_{\mathcal{F}}(p, q_\theta) = -\mathbb{E}_{z, c} [J_{G_\theta}(z, c)^\top \nabla_x f_{\psi^*}(G_\theta(c, z))]. \quad (46)$$

If instead \mathcal{F} is the full 1-Lipschitz ball (Wasserstein-1), the above expression defines a subgradient (with the same leading minus sign) for any measurable selection $f^* \in \arg \max_{f \in \mathcal{F}} (\mathbb{E}_p f - \mathbb{E}_{q_\theta} f)$.

Proof. This is Assumption 5 for $G_\theta(c, z)$ with compact \mathcal{F} ; see also standard IPM/Wasserstein results [2, 3, 72]. \square

Theorem 4 (First-Order Stationarity). *Under Assumption 10 and Lemma 4, any stationary point θ^\dagger (gradient or, for W_1 , subgradient) of Equation 45 satisfies*

$$\begin{aligned} -\lambda \mathbb{E} [J_G^\top \nabla_x f^*(G)] &+ 2\alpha \mathbb{E} [J_G^\top (G - x)] \\ &+ 2\beta \mathbb{E} [J_G^\top J_\Phi^\top (\Phi(G) - \Phi(x))] = 0, \end{aligned} \quad (47)$$

with $G = G_{\theta^\dagger}(c, z)$, $J_G = J_{G_{\theta^\dagger}}(c, z)$, J_Φ evaluated at G .

7.3. Off-Manifold Control and “Sharpness Ceiling”

We formalize two key effects of Equation 45: (i) off-manifold suppression via the IPM term and (ii) bounded over-sharpening relative to p (“sharpness ceiling”).

Proposition 8 (Off-manifold penalty via W_1 tube bound).

Let $\mathcal{M} = \text{supp}(p)$ and $\mathcal{N}_\alpha(\mathcal{M}) = \{x : \text{dist}(x, \mathcal{M}) \leq \alpha\}$. If $q_\theta(\mathcal{N}_\alpha(\mathcal{M})) \leq 1 - \mu_\alpha$, then

$$W_1(p, q_\theta) \geq \alpha \mu_\alpha. \quad (48)$$

Thus any nontrivial mass placed outside an α -tube around the natural-image manifold induces at least $\alpha \mu_\alpha$ Wasserstein cost.

Proof. By the Kantorovich–Rubinstein duality, $W_1(p, q_\theta) = \sup_{\|f\|_{\text{Lip}} \leq 1} \{\mathbb{E}_p f - \mathbb{E}_{q_\theta} f\}$. Let $f(x) = \min\{\text{dist}(x, \mathcal{M}), \alpha\}$, which is 1-Lipschitz. Then $f \equiv 0$ on \mathcal{M} and $f(x) \geq \alpha$ for $x \notin \mathcal{N}_\alpha(\mathcal{M})$. Take $g = -f$, also 1-Lipschitz. Then:

$$\mathbb{E}_p g - \mathbb{E}_{q_\theta} g = -\mathbb{E}_p f + \mathbb{E}_{q_\theta} f \geq 0 + \alpha \mu_\alpha = \alpha \mu_\alpha. \quad (49)$$

Hence $W_1(p, q_\theta) \geq \alpha \mu_\alpha$. See [2]. \square

Proposition 9 (Sharpness Ceiling via 1-Lipschitz Functionals). Let $d_{\mathcal{F}} = W_1$ (or more generally suppose there exists $c_{\mathcal{F}} > 0$ such that $d_{\mathcal{F}} \geq c_{\mathcal{F}} W_1$). Let $T : \mathcal{X} \rightarrow \mathcal{Y}$ be linear with $\|T\| \leq 1$. Then, for $f(x) = \|Tx\|_2$ (1-Lipschitz),

$$d_{\mathcal{F}}(p, q_\theta) \geq c_{\mathcal{F}} |\mathbb{E}_p \|Tx\|_2 - \mathbb{E}_{q_\theta} \|T\tilde{x}\|_2|. \quad (50)$$

Specifically, any deliberate amplification of band-/high-pass components—i.e., applying T as a band-pass filter or gradient—forces an increase in $d_{\mathcal{F}}$, providing a distributional upper bound for over-sharpening.

Proof. Since f is 1-Lipschitz, the Kantorovich–Rubinstein dual implies $W_1(p, q_\theta) \geq \mathbb{E}_p f - \mathbb{E}_{q_\theta} f$ [2]. Applying the same argument with $-f$ establishes the reverse inequality and yields the absolute difference. Using $d_{\mathcal{F}} \geq c_{\mathcal{F}} W_1$ gives Equation 50. \square

7.4. Perceptual Anchoring: Deviation Bounds

We next show that, even without explicit data-consistency, the paired pixel/perceptual terms constrain nullspace-like deviations (including directions weakly reflected by H) because they are measured against the ground-truth x .

Proposition 10 (Component-wise control by the pixel term). Let $P : \mathcal{X} \rightarrow \mathcal{X}$ be any nonexpansive linear projector ($\|P\| \leq 1$). With the α used in Equation 45,

$$\mathbb{E} \|P(G_\theta(c, z) - x)\|_2^2 \leq \frac{1}{\alpha} \mathcal{J}(\theta). \quad (51)$$

At any minimizer θ^* , $\mathbb{E} \|P(G_{\theta^*} - x)\|_2^2 \leq \inf_\theta \mathcal{J}(\theta) / \alpha$.

Proof. From Equation 45, one obtains $\mathcal{J}(\theta) \geq \alpha \mathbb{E} \|G_\theta - x\|^2 \geq \alpha \mathbb{E} \|P(G_\theta - x)\|^2$, where the second inequality follows from the contractive property $\|P\| \leq 1$. \square

Proposition 11 (Perceptual Alignment Controls Feature-Space Deviations). For any Φ ,

$$\mathbb{E} \|\Phi(G_\theta) - \Phi(x)\|_2^2 \leq \frac{1}{\beta} \mathcal{J}(\theta). \quad (52)$$

Moreover, whenever Φ dominates a high-frequency semi-norm Π (i.e., $\Pi(u) \leq C \|\Phi(u)\|_2$ for u in the region of interest), we obtain

$$\begin{aligned} \mathbb{E} \Pi(G_\theta - x) &\leq C \left(\mathbb{E} \|\Phi(G_\theta) - \Phi(x)\|_2^2 \right)^{1/2} \\ &\leq \frac{C}{\sqrt{\beta}} \sqrt{\mathcal{J}(\theta)}. \end{aligned} \quad (53)$$

Hence feature-space alignment upper-bounds perceptual/high-frequency deviations.

7.5. No Over-Generation at Optimum

We combine IPM and pixel/perceptual anchoring to show that stationary solutions cannot produce arbitrarily exaggerated details relative to p and x .

Theorem 5 (Combined Control of Over-Generation). Assume $d_{\mathcal{F}} = W_1$ (or, more generally, there exists $c_{\mathcal{F}} > 0$ such that $d_{\mathcal{F}} \geq c_{\mathcal{F}} W_1$). Let T be linear with $\|T\| \leq 1$, and let P be any projector with $\|P\| \leq 1$. Then, for any θ ,

$$\begin{aligned} |\mathbb{E}_{q_\theta} \|T\tilde{x}\|_2 - \mathbb{E}_p \|Tx\|_2| &\leq \frac{1}{\lambda c_{\mathcal{F}}} \mathcal{J}(\theta), \\ \mathbb{E} \|P(G_\theta - x)\|_2^2 &\leq \frac{1}{\alpha} \mathcal{J}(\theta), \end{aligned} \quad (54)$$

and

$$\mathbb{E} \|\Phi(G_\theta) - \Phi(x)\|_2 \leq \frac{1}{\sqrt{\beta}} \sqrt{\mathcal{J}(\theta)}. \quad (55)$$

In particular, at any global minimizer θ^* , all three deviations are jointly minimized and cannot be simultaneously large. Thus, the adversarial training is biased toward faithful reconstructions (natural-manifold and feature-aligned), lacking the tendency to over-generate ultra-sharp details.

7.6. From AR/FM Biases to Adversarial Training Fidelity

Theorem 6 (Fidelity Guarantees for Low-Level Restoration). Consider $c = Hx + \eta$ under the spectral/regularity assumptions in Sections 6–7.5 of the Appendix, and let $p(x | c)$ denote the ground-truth posterior. Suppose generators are trained with: (1) conditional AR MLE (Equation 12); (2) FM Fisher minimization (Equation 13); (3) a composite adversarial training objective (Equation 45).

1. **Autoregression (AR).** Single-mode conditional factorization together with greedy or vanishing-temperature decoding enforces a deterministic resolution of posterior ambiguity along $\ker H$: genuinely distinct posterior modes contract toward midpoints, reducing variability and introducing structured artifacts. Under teacher forcing with test-time rollout, the total-variation discrepancy can accumulate up to linear order with sequence length in the worst case (Lemma 1), yielding distortions and over-generation [5, 44, 62, 66].
2. **Flow Matching (FM).** FM minimizes an integral of conditional Fisher divergences of Gaussian-smoothed posteriors with effective frequency weight:

$$\widetilde{W}_t(\omega) \propto \|\omega\|^2 e^{-\sigma_t^2 \|\omega\|^2} \Xi_t(\omega).$$

Exponential high-frequency damping and null bands where $\Xi_t(\omega)$ is tiny (including $|\hat{H}(\omega)| = 0$) make FM insensitive to null-space errors, weak on textures/edges, and amplify local drifts into macroscopic warps or hallucinations [23, 45, 46, 70].

3. **Adversarial Training.** The composite objective enforces: (i) distributional alignment via an IPM critic, suppressing off-manifold mass; (ii) pixel-space anchoring to the ground truth, which bounds all measurable components of x ; and (iii) perceptual alignment in feature space, which regulates high-frequency discrepancies. At any global minimizer these constraints hold jointly, yielding sharp, faithful reconstructions without uncontrolled over-generation [2, 3, 72].

The preceding sections have established complementary theoretical limitations of autoregressive (AR) and flow matching (FM) objectives in the low-level restoration setting. For AR, the conditional factorization and single-mode decoding force posterior ambiguities in $\ker(H)$ to collapse deterministically, while exposure bias causes small local mismatches to accumulate into global artifacts and over-generation. For FM, the Fisher-based objective is spectrally reweighted by Gaussian smoothing and the forward operator (through Ξ_t), which underweights high-frequency errors, ignores $\ker(H)$ components, and allows unconditional textures to leak in at early times; small drift errors near edges are then amplified into visible warps. In contrast, the adversarial training formulation explicitly combines three complementary forces: (i) distributional alignment with the natural-image manifold via an IPM critic, (ii) pixel-level fidelity to the ground truth, and (iii) perceptual alignment in feature space. These terms jointly prevent both collapse and uncontrolled hallucination, while maintaining sharpness without exceeding the statistics of p .

Together, these complementary objectives provide a precise characterization of fidelity and stability (Theorem 6).

8. Frequency-Aware Low-Level Instructions

Universal Restoration Instruction r .

```
Analyze and return 1 line: Task: <task_token>,
Focus: <high | low>, Rationale: <brief reason>,
Pipeline: <step1 -> step2 -> ....>.
```

Interpretation. The role of r is to constrain the planner’s output format and scope: it precludes free-form text, enforces a single categorical decision, ties that decision to an interpretable frequency regime, and requires both a concise rationale and a stepwise restoration plan.

Expert Rule P_{expert} .

```
You are an expert image restoration task classifier.
Available tasks (use EXACT lowercase tokens):
deraining | desnowing | dehazing | deblur | denoise
| light_enhancement | super_resolution.

Critical distinctions:
RAIN (deraining)
- Linear streaks: parallel/near-parallel elongated lines
- Overlay effect: streaks cross sharp edges without blurring them
- Directional: consistent orientation (diagonal/vertical)
- Can coexist with low contrast, but streaks are visible as distinct overlays
SNOW (desnowing)
- Particles: round/irregular white blobs, bokeh discs
- Size variation: larger near, smaller far
- Random distribution, NOT linear/parallel
HAZE (dehazing)
- Depth-dependent: far objects more degraded than near
- Milky appearance with desaturation
- Distance gradient clearly visible
BLUR (deblur)
- Edge smearing: boundaries themselves are widened/soft
- Uniform softness or motion trails
- Object edges lose geometric precision
NOISE (denoise)
- Grain on crisp edges: edge structure intact but covered by speckles
- Random texture in flat areas
- High-ISO appearance
UNDEREXPOSED (light_enhancement)
- Globally dark, no depth gradient
- Histogram left-biased, shadows crushed
- Color cast possible
LOW RESOLUTION (super_resolution)
- Insufficient spatial sampling: small native  $H \times W$  or strong aliasing
- Loss of fine textures; blockiness/jagged edges when upscaled
- Distinct from blur: edges can appear jagged/aliased rather than uniformly smeared
Frequency decision rules:
Choose high when degradation is dominated by fine-scale artifacts or missing detail that lives in high spatial frequencies:
- deblur (recover sharp edges and textures)
- denoise (suppress noisy high-frequency speckles while preserving true details)
- deraining / desnowing (remove thin streaks/particles and recover edge micro-structure)
Choose low when degradation is dominated by global/slow-varying components:
```

```

- dehazing (restore low-frequency contrast/airlight;
depth-dependent veiling)
- light_enhancement (global exposure/illumination
and tone mapping)

If signals suggest mixed conditions, choose the
dominant component according to the most visible
impairment.

Pipeline rules:
- DO NOT use any task names in the Pipeline.

```

Interpretation. P_{expert} formalizes image restoration as a frequency-aware understanding problem, aligning perceptual degradations with their dominant spectral signatures. It specifies a principled decision boundary: fine-scale losses, rain, snow, noise, blur, map to high-frequency restoration, whereas global, slowly varying degradations, haze, illumination, map to low-frequency correction. By explicitly treating super-resolution as a sampling-limited case, P_{expert} extends the taxonomy beyond semantic labels toward signal-reconstruction logic. Building on this prior, the planner emits, for each instance, an auditable reasoning trace and an executable restoration plan that directly guide the downstream executor.

Label-free Low-level Feature Pool P_{hints} .

```

Use the following label-free features computed from
image pixels to support your decision.

Image size:  $H, W$  (pixels). Include scale cues for
potential super_resolution.

(1) Rain cues  $\phi_{\text{rain}}$ : Grad. orientation: grayscale
 $g \in [0, 1]$ ,  $(g_x, g_y)$ , magnitude  $m = \sqrt{g_x^2 + g_y^2}$ ;
 $\theta = \text{mod}(\arctan 2(g_y, g_x), \pi)$ ; weighted histogram  $h(\theta)$ 
with weights  $m$ . Scores: line_score=  $\max h / \sum h$ ,
anisotropy=  $(\max h - \text{mean } h) / (\text{mean } h)$ . Spectrum:
power  $P$  from FFT of  $g$ ; annuli (mid/low) by radius;
freq_ratio=  $\text{mean}(P_{\text{mid}}) / (\text{mean}(P_{\text{low}}) + \varepsilon)$ .

(2) Snow cues  $\phi_{\text{snow}}$ : Blobs:  $b = \mathbb{1}[g > 0.78]$ ;
connected components; small_blobs=  $\#\{3 \leq \text{area} \leq 200\}$ .
Isotropy: reuse  $h(\theta)$ ; lower anisotropy  $\rightarrow$  more
snow-like randomness.

(3) Noise cues  $\phi_{\text{noise}}$ : Flat mask:  $\Omega_{\text{flat}} = \{m < Q_{0.25}(m)\}$ ; local mean  $\bar{g}$  (box  $3 \times 3$ ); residual
 $r = g - \bar{g}$ . Stats: noise_mad=  $\text{median}(|r - \text{median}(r)|)$ .
Chroma: YCbCr std on  $\Omega_{\text{flat}}$ , chroma_std=  $\frac{1}{2}(\text{std}(C_b) + \text{std}(C_r))$ . Score: noise_score=  $0.6\sigma(50(\text{noise_mad} - 0.0050)) + 0.4\sigma(50(\text{chroma_std} - 0.0095))$ .

(4) Blur cues  $\phi_{\text{blur}}$ : Laplacian var:  $\text{lapVar} = \text{Var}(L * g)$ . Spectrum ratio: hf_energy=
 $\text{mean}(P_{\text{outer}}) / (\text{mean}(P_{\text{inner}}) + \varepsilon)$ . Edge strength:
 $\text{grad95} = Q_{0.95}(\sqrt{g_{x,s}^2 + g_{y,s}^2})$  with mild smoothing.

(5) Haze cues  $\phi_{\text{haze}}$ : Dark channel: dark_mean=
 $\text{mean}(\min(R, G, B))$ ; Saturation: sat_mean=  $\text{mean}(S)$ 
in HSV. Depth proxy: split top/bottom;
 $\text{depth\_grad} = \text{mean}(Y_{\text{top}}) - \text{mean}(Y_{\text{bot}})$ . Composite:
haze_score=  $0.4\sigma(7(\text{dark_mean} - 0.33)) + 0.3\sigma(7(0.30 - \text{sat_mean})) + 0.3\sigma(8(\text{depth\_grad} - 0.03))$ .

(6) Exposure cues  $\phi_{\text{expo}}$ : Luma stats: meanY=
 $\text{mean}(Y)$ ,  $p50 = Q_{0.50}(Y)$ ; underexposed if  $\text{meanY} < 0.32$ 
or  $p50 < 0.26$ .

Recommended thresholds (for disambiguation): Rain:
line_score> 0.16, anisotropy> 0.40, freq_ratio> 1.05;
Snow: small_blobs> 25, anisotropy< 0.42. Noise:
noise_score> 0.45; Blur: grad95< 0.17, lapVar< 0.27,
hf_energy< 0.052. Haze: haze_score> 0.50,
depth_grad> 0.03; Underexp: meanY< 0.32 or
p50< 0.26.

```

```

Example (auto-filled at runtime): Rain: line=0.21,
aniso=0.45, freq=1.08; Snow: blobs=31, aniso=0.38;
Noise: mad=0.0061, chroma=0.0083, score=0.47;
Blur: lapVar=0.256, hf=0.055, grad95=0.174; Haze:
score=0.42, depth_grad=0.028, dark_mean=0.36,
sat_mean=0.29; Exposure: meanY=0.31, p50=0.27;
Size: H=480, W=320.

```

Interpretation. P_{hints} grounds each decision in measurable, pixel-level evidence, making the planner’s reasoning traceable and reproducible. Gradient orientation, spectrum energy ratios, and brightness statistics are mapped to specific degradation cues, translating physical image phenomena into quantitative signals. High-frequency degradations (rain, snow, noise, blur) and low-frequency ones (haze, exposure) are thus separated by data-driven thresholds, while image size provides an explicit trigger for super-resolution. This turns frequency focus from a heuristic label into a verifiable diagnostic built on interpretable computational cues.

9. Detailed Metrics

To complement the main quantitative comparison in Table 1 and Table 2, we provide full per-benchmark results in Table 5 and Table 6 of the appendix. These tables report all five distortion–perception metrics (PSNR, SSIM, LPIPS, FID, DISTs) for each individual benchmark across seven restoration tasks (deraining, desnowing, dehazing, deblurring, denoising, low-light enhancement, and super-resolution), together with a unified comparison against recent AIO-IR methods [15, 34, 58, 78, 109] and SR baselines [41, 83, 92, 97, 98, 103]. Overall, FAPE-IR attains state-of-the-art or comparable performance on the majority of benchmarks, especially on weather-related degradations and challenging real-world benchmarks, where it substantially improves both PSNR/SSIM and perceptual metrics.

In the high-frequency-dominant restoration regimes (e.g., OutDoor, RainDrop, Snow100K-L/S, Rain100_H, GoPro-gamma, RealBlur-J/R, Urban100-15/25/50), our method consistently attains markedly lower LPIPS and DISTs together with competitive or clearly higher PSNR/FID than prior AIO-IR approaches, indicating that the frequency-aware planner and band-specialized LoRA-MoE executor effectively suppress artifacts while preserving fine structures. In contrast, for low-frequency degradations such as URHI, ITS-val, and LOL-v1/v2, FAPE-IR achieves strong gains in FID and DISTs while maintaining high SSIM, reflecting better global contrast and color consistency under severe haze and illumination changes. A remaining challenge lies in Rain100_L and the BSD68-15/25/50 denoising benchmarks, where FAPE-IR is less competitive in PSNR. We attribute this mainly to a mismatch between our training distribution and these relatively simple degradations (light rain and synthetic Gaussian noise), together with the limited amount of pure denoising data: the planner tends to favor stronger high-frequency

Table 5. Unified quantitative comparison across all benchmarks. Our method (**FAPE-IR**) consistently achieves state-of-the-art or comparable performance across diverse restoration benchmarks.

Method	OutDoor				RainDrop				Rain100_L				Rain100_H							
	PSNR↑	SSIM↑	LPIPS↓	FID↓	DISTS↓	PSNR↑	SSIM↑	LPIPS↓	FID↓	DISTS↓	PSNR↑	SSIM↑	LPIPS↓	FID↓	DISTS↓	PSNR↑	SSIM↑	LPIPS↓	FID↓	DISTS↓
<i>State-of-the-art AIO-IR methods</i>																				
PromptIR [58]	18.40	0.67	0.41	154.96	0.30	23.48	0.80	0.18	61.42	0.12	37.41	0.98	0.02	8.84	0.03	15.93	0.52	0.46	175.42	0.27
FoundIR [34]	17.07	0.65	0.45	156.17	0.30	23.52	0.80	0.21	63.57	0.14	30.62	0.93	0.11	34.19	0.08	13.77	0.43	0.55	219.48	0.33
DFPIR [78]	14.06	0.60	0.50	176.41	0.38	22.52	0.79	0.20	64.91	0.14	37.99	0.98	0.02	8.25	0.03	16.07	0.54	0.44	166.89	0.26
MoCE-IR [109]	17.99	0.67	0.41	154.87	0.30	23.30	0.80	0.18	61.89	0.12	38.05	0.98	0.02	7.90	0.02	15.33	0.49	0.48	180.16	0.28
AdaIR [15]	18.23	0.67	0.41	155.67	0.30	23.37	0.80	0.18	61.89	0.12	38.00	0.98	0.02	7.58	0.02	15.93	0.52	0.46	175.01	0.27
Ours	28.16	0.83	0.09	25.16	0.07	25.83	0.80	0.11	20.86	0.11	33.18	0.93	0.04	10.21	0.03	27.01	0.82	0.13	33.58	0.09
Method	BSD68-15				BSD68-25				BSD68-50				Urban100-15							
	PSNR↑	SSIM↑	LPIPS↓	FID↓	DISTS↓	PSNR↑	SSIM↑	LPIPS↓	FID↓	DISTS↓	PSNR↑	SSIM↑	LPIPS↓	FID↓	DISTS↓	PSNR↑	SSIM↑	LPIPS↓	FID↓	DISTS↓
<i>State-of-the-art AIO-IR methods</i>																				
PromptIR [58]	28.60	0.85	0.20	49.74	0.14	27.15	0.72	0.32	86.65	0.21	23.52	0.48	0.52	164.09	0.33	38.98	0.98	0.01	5.28	0.05
FoundIR [34]	33.87	0.88	0.17	49.61	0.12	29.81	0.75	0.29	85.98	0.19	23.99	0.50	0.50	160.78	0.31	36.90	0.97	0.03	10.50	0.07
DFPIR [78]	30.78	0.88	0.15	45.11	0.11	28.41	0.75	0.28	81.08	0.19	23.42	0.49	0.50	161.16	0.31	37.80	0.97	0.03	11.79	0.08
MoCE-IR [109]	29.78	0.84	0.20	49.93	0.14	27.11	0.71	0.32	85.49	0.21	23.32	0.48	0.52	163.59	0.32	39.19	0.98	0.01	6.16	0.05
AdaIR [15]	29.58	0.84	0.20	49.85	0.13	27.51	0.71	0.32	85.31	0.21	23.34	0.48	0.52	164.68	0.33	38.94	0.98	0.02	6.11	0.05
Ours	34.21	0.91	0.09	26.94	0.07	31.79	0.85	0.15	44.19	0.11	27.87	0.72	0.27	76.01	0.17	31.09	0.93	0.02	7.45	0.05
Method	Urban100-25				Urban100-50				ITS-val				URHI							
	PSNR↑	SSIM↑	LPIPS↓	FID↓	DISTS↓	PSNR↑	SSIM↑	LPIPS↓	FID↓	DISTS↓	PSNR↑	SSIM↑	LPIPS↓	FID↓	DISTS↓	PSNR↑	SSIM↑	LPIPS↓	FID↓	DISTS↓
<i>State-of-the-art AIO-IR methods</i>																				
PromptIR [58]	35.36	0.96	0.02	9.37	0.06	29.40	0.89	0.08	31.77	0.12	21.51	0.89	0.15	37.38	0.11	26.18	0.95	0.05	11.30	0.05
FoundIR [34]	32.72	0.90	0.09	27.28	0.12	26.29	0.72	0.30	68.30	0.22	13.32	0.74	0.33	49.35	0.22	16.99	0.84	0.17	19.74	0.14
DFPIR [78]	34.35	0.94	0.05	21.67	0.10	29.52	0.84	0.13	49.97	0.17	12.42	0.71	0.32	47.00	0.23	24.64	0.94	0.06	11.97	0.05
MoCE-IR [109]	35.78	0.97	0.02	10.39	0.07	29.94	0.92	0.06	24.88	0.11	14.71	0.79	0.24	43.64	0.16	23.76	0.93	0.07	12.32	0.06
AdaIR [15]	35.53	0.96	0.02	9.14	0.06	29.36	0.89	0.09	33.24	0.13	19.44	0.87	0.17	39.66	0.13	24.46	0.94	0.06	11.83	0.05
Ours	30.17	0.91	0.03	9.93	0.06	27.82	0.86	0.06	17.44	0.09	34.07	0.97	0.04	6.11	0.04	31.62	0.96	0.04	8.31	0.04
Method	Snow100K-L				Snow100K-S				GoPro				GoPro-gamma							
	PSNR↑	SSIM↑	LPIPS↓	FID↓	DISTS↓	PSNR↑	SSIM↑	LPIPS↓	FID↓	DISTS↓	PSNR↑	SSIM↑	LPIPS↓	FID↓	DISTS↓	PSNR↑	SSIM↑	LPIPS↓	FID↓	DISTS↓
<i>State-of-the-art AIO-IR methods</i>																				
AdaIR [15]	21.03	0.70	0.32	38.69	0.19	27.40	0.84	0.21	14.87	0.12	29.03	0.87	0.18	24.94	0.12	27.96	0.86	0.19	28.49	0.12
FoundIR [34]	20.89	0.73	0.33	39.96	0.20	26.72	0.84	0.23	18.99	0.15	27.51	0.81	0.24	39.35	0.16	27.21	0.81	0.24	41.79	0.16
DFPIR [78]	18.41	0.67	0.35	48.50	0.21	23.18	0.81	0.25	21.14	0.15	30.09	0.89	0.16	21.59	0.10	28.84	0.88	0.17	25.59	0.11
MoCE-IR [109]	21.00	0.69	0.33	43.21	0.20	26.67	0.83	0.23	17.74	0.13	29.56	0.90	0.16	20.10	0.10	27.93	0.87	0.18	25.85	0.11
Ours	29.07	0.85	0.10	18.88	0.07	31.52	0.90	0.06	11.00	0.05	28.13	0.84	0.13	16.04	0.08	28.00	0.84	0.13	17.13	0.08
Method	RealBlur-J				RealBlur-R				LOL-v2				LOL-v1							
	PSNR↑	SSIM↑	LPIPS↓	FID↓	DISTS↓	PSNR↑	SSIM↑	LPIPS↓	FID↓	DISTS↓	PSNR↑	SSIM↑	LPIPS↓	FID↓	DISTS↓	PSNR↑	SSIM↑	LPIPS↓	FID↓	DISTS↓
<i>State-of-the-art AIO-IR methods</i>																				
AdaIR [15]	17.74	0.71	0.28	51.66	0.18	12.54	0.51	0.51	93.48	0.36	24.48	0.86	0.18	48.78	0.13	24.93	0.92	0.12	52.78	0.11
FoundIR [34]	28.27	0.85	0.19	40.88	0.15	30.66	0.93	0.15	46.12	0.18	14.44	0.66	0.33	77.47	0.23	14.54	0.75	0.28	95.49	0.21
DFPIR [78]	28.75	0.87	0.16	29.58	0.12	36.00	0.96	0.10	36.17	0.14	25.92	0.90	0.16	50.62	0.13	25.95	0.92	0.12	53.66	0.11
MoCE-IR [109]	15.76	0.68	0.30	52.80	0.19	11.55	0.48	0.53	96.66	0.37	23.25	0.89	0.16	44.31	0.12	24.93	0.92	0.11	44.90	0.09
Ours	30.56	0.87	0.10	18.21	0.07	37.77	0.97	0.05	14.74	0.07	25.07	0.90	0.11	32.94	0.09	28.95	0.92	0.11	47.67	0.09
Method	RealSR 2x				DrealSR 2x				RealSR 4x				DrealSR 4x							
	PSNR↑	SSIM↑	LPIPS↓	FID↓	DISTS↓	PSNR↑	SSIM↑	LPIPS↓	FID↓	DISTS↓	PSNR↑	SSIM↑	LPIPS↓	FID↓	DISTS↓	PSNR↑	SSIM↑	LPIPS↓	FID↓	DISTS↓
<i>State-of-the-art SR methods</i>																				
StableSR [83]	24.22	0.75	0.23	81.72	0.19	25.71	0.75	0.26	91.11	0.18	23.11	0.68	0.30	127.06	0.22	27.63	0.73	0.35	140.86	0.23
DiffBIR [41]	26.31	0.71	0.30	80.60	0.21	27.31	0.70	0.37	103.44	0.24	23.75	0.62	0.37	131.16	0.24	25.49	0.57	0.52	182.95	0.31
SeeSR [98]	25.90	0.75	0.28	100.75	0.22	28.05	0.77	0.30	107.08	0.23	24.05	0.69	0.32	128.56	0.24	28.78	0.77	0.34	152.01	0.25
PASD [103]	26.19	0.76	0.24	92.31	0.19	27.96	0.77	0.27	107.73	0.20	24.69	0.71	0.31	131.09	0.21	28.97	0.78	0.33	150.68	0.22
OSEDiff [97]	25.56	0.76	0.25	100.26	0.20	27.37	0.79	0.27	114.31	0.20	24.51	0.72	0.30	124.37	0.21	28.84	0.79	0.31	131.27	0.22
PURE [92]	23.59	0.65	0.32	83.81	0.22	25.84	0.68	0.37	108.30	0.23	22.20	0.59	0.39	127.72	0.25	26.53	0.64	0.44	158.88	0.26
Ours	29.99	0.88	0.13	51.05	0.12	30.52	0.89	0.14	60.30	0.12	25.55	0.78	0.24	105.75	0.19	28.42	0.84	0.25	126.45	0.19

suppression, which can lead to slight over-smoothing and thus lower PSNR on texture-rich scenes, while still preserving favorable perceptual metrics.

Table 6 further reports no-reference image quality metrics on the same set of benchmarks. Across most restoration benchmarks (excluding SR), FAPE-IR improves or matches the best scores on at least three of the five IQA indicators, confirming that our adversarial training and frequency regularization translate into reconstructions that are also preferred by hand-crafted NR-IQA measures. For real-world super-resolution, however, FAPE-IR exhibits a different pattern: while Table 5 shows clear advantages in full-reference distortion and perceptual metrics (PSNR/SSIM, LPIPS, FID, DISTs), the no-reference scores in Table 6 are sometimes worse than those of competing SR methods. We speculate that this discrepancy stems from the SR ground-

truth images themselves, whose statistics yield relatively poor scores under standard NR-IQA metrics. By recovering textures and statistics closer to these ground truths, FAPE-IR improves full-reference and

Table 6. Unified quantitative comparison across all benchmarks. Our method (**FAPE-IR**) consistently achieves state-of-the-art or comparable performance across diverse restoration benchmarks.

Method	OutDoor					RainDrop					Rain100_L					Rain100_H				
	NIQE↓	MUSIQ↑	MANIQA↑	CLIPQA↑	TOPIQ↑	NIQE↓	MUSIQ↑	MANIQA↑	CLIPQA↑	TOPIQ↑	NIQE↓	MUSIQ↑	MANIQA↑	CLIPQA↑	TOPIQ↑	NIQE↓	MUSIQ↑	MANIQA↑	CLIPQA↑	TOPIQ↑
<i>State-of-the-art AIO-IR methods</i>																				
PromPIR [58]	4.59	69.40	0.68	0.69	0.50	6.68	61.27	0.58	0.45	0.39	7.18	59.42	0.58	0.31	0.46	3.16	65.43	0.66	0.46	0.51
FoundIR [34]	4.76	68.41	0.67	0.63	0.48	8.48	60.45	0.57	0.38	0.41	6.32	61.27	0.57	0.32	0.40	3.65	67.02	0.66	0.42	0.50
DFPIR [78]	4.60	69.64	0.68	0.70	0.50	6.38	61.81	0.59	0.46	0.40	6.87	57.64	0.52	0.28	0.40	3.17	64.49	0.65	0.42	0.50
MoCE-IR [109]	4.59	69.74	0.68	0.70	0.50	7.20	62.47	0.59	0.46	0.41	7.11	58.90	0.58	0.29	0.47	3.21	65.56	0.66	0.45	0.52
AdaIR [15]	4.60	69.67	0.68	0.70	0.50	6.89	61.96	0.59	0.45	0.40	7.19	58.95	0.58	0.29	0.48	3.15	65.35	0.66	0.49	0.51
Ours	5.04	69.34	0.68	0.67	0.48	5.04	66.57	0.64	0.61	0.45	3.42	68.26	0.68	0.39	0.58	2.99	69.12	0.70	0.46	0.55
Method	BSD68-15					BSD68-25					BSD68-50					Urban100-15				
	NIQE↓	MUSIQ↑	MANIQA↑	CLIPQA↑	TOPIQ↑	NIQE↓	MUSIQ↑	MANIQA↑	CLIPQA↑	TOPIQ↑	NIQE↓	MUSIQ↑	MANIQA↑	CLIPQA↑	TOPIQ↑	NIQE↓	MUSIQ↑	MANIQA↑	CLIPQA↑	TOPIQ↑
<i>State-of-the-art AIO-IR methods</i>																				
PromPIR [58]	5.25	45.68	0.57	0.55	0.33	5.71	39.01	0.54	0.47	0.30	5.33	72.86	0.52	0.38	0.28	5.33	72.86	0.75	0.62	0.73
FoundIR [34]	5.34	46.89	0.57	0.58	0.34	5.80	40.08	0.55	0.50	0.31	7.32	37.11	0.52	0.43	0.30	4.25	71.22	0.72	0.61	0.67
DFPIR [78]	5.27	48.63	0.57	0.60	0.35	5.66	42.49	0.55	0.54	0.33	7.05	39.04	0.52	0.45	0.32	5.57	73.52	0.76	0.67	0.73
MoCE-IR [109]	5.38	46.03	0.57	0.55	0.33	5.80	39.04	0.55	0.47	0.30	7.12	35.44	0.52	0.39	0.28	5.46	73.08	0.75	0.63	0.74
AdaIR [15]	5.30	45.57	0.57	0.56	0.33	5.76	38.84	0.55	0.46	0.30	7.11	35.16	0.52	0.39	0.28	5.20	72.78	0.75	0.63	0.73
Ours	5.13	51.60	0.58	0.64	0.36	4.87	49.24	0.56	0.50	0.34	4.64	44.90	0.74	0.64	0.70	4.90	72.17	0.74	0.64	0.70
Method	Urban100-25					Urban100-50					ITS-val					URHI				
	NIQE↓	MUSIQ↑	MANIQA↑	CLIPQA↑	TOPIQ↑	NIQE↓	MUSIQ↑	MANIQA↑	CLIPQA↑	TOPIQ↑	NIQE↓	MUSIQ↑	MANIQA↑	CLIPQA↑	TOPIQ↑	NIQE↓	MUSIQ↑	MANIQA↑	CLIPQA↑	TOPIQ↑
<i>State-of-the-art AIO-IR methods</i>																				
PromPIR [58]	4.79	72.39	0.74	0.61	0.72	4.11	70.23	0.68	0.56	0.68	4.53	51.32	0.50	0.10	0.35	4.21	54.28	0.64	0.27	0.35
FoundIR [34]	3.86	66.26	0.69	0.58	0.61	4.34	55.79	0.63	0.54	0.50	5.65	49.82	0.50	0.14	0.36	5.16	54.44	0.63	0.30	0.35
DFPIR [78]	5.86	73.15	0.76	0.64	0.69	7.13	69.97	0.71	0.58	0.56	5.10	46.81	0.48	0.11	0.34	4.16	54.11	0.63	0.24	0.35
MoCE-IR [109]	5.54	73.36	0.75	0.60	0.73	4.80	72.46	0.73	0.56	0.69	5.01	49.54	0.49	0.11	0.36	4.24	54.34	0.63	0.27	0.36
AdaIR [15]	5.01	72.75	0.75	0.62	0.72	4.13	69.45	0.68	0.58	0.67	4.65	50.44	0.49	0.10	0.34	4.22	54.20	0.63	0.28	0.35
Ours	4.92	71.90	0.73	0.62	0.69	4.96	70.73	0.70	0.57	0.66	5.66	47.88	0.55	0.13	0.30	4.47	53.76	0.64	0.23	0.35
Method	Snow100K-L					Snow100K-S					GoPro					GoPro-gamma				
	NIQE↓	MUSIQ↑	MANIQA↑	CLIPQA↑	TOPIQ↑	NIQE↓	MUSIQ↑	MANIQA↑	CLIPQA↑	TOPIQ↑	NIQE↓	MUSIQ↑	MANIQA↑	CLIPQA↑	TOPIQ↑	NIQE↓	MUSIQ↑	MANIQA↑	CLIPQA↑	TOPIQ↑
<i>State-of-the-art AIO-IR methods</i>																				
AdaIR [15]	3.61	55.64	0.63	0.42	0.42	3.56	60.12	0.66	0.47	0.46	4.86	46.63	0.57	0.22	0.31	4.90	45.67	0.56	0.21	0.30
FoundIR [34]	4.53	57.99	0.64	0.39	0.42	4.56	62.57	0.67	0.43	0.46	5.24	40.86	0.49	0.22	0.26	5.25	41.06	0.50	0.22	0.26
DFPIR [78]	4.09	54.86	0.62	0.39	0.41	3.99	59.47	0.65	0.43	0.44	4.73	50.62	0.60	0.23	0.34	4.79	49.54	0.59	0.22	0.33
MoCE-IR [109]	3.85	55.91	0.63	0.38	0.42	3.76	60.54	0.66	0.43	0.46	4.61	51.14	0.60	0.25	0.35	4.70	48.42	0.58	0.23	0.33
Ours	3.66	62.51	0.66	0.41	0.45	3.55	63.57	0.67	0.43	0.47	4.33	53.83	0.61	0.24	0.39	4.32	53.91	0.60	0.24	0.40
Method	RealBlur-J					RealBlur-R					LOL-v2					LOL-v1				
	NIQE↓	MUSIQ↑	MANIQA↑	CLIPQA↑	TOPIQ↑	NIQE↓	MUSIQ↑	MANIQA↑	CLIPQA↑	TOPIQ↑	NIQE↓	MUSIQ↑	MANIQA↑	CLIPQA↑	TOPIQ↑	NIQE↓	MUSIQ↑	MANIQA↑	CLIPQA↑	TOPIQ↑
<i>State-of-the-art AIO-IR methods</i>																				
AdaIR [15]	5.17	42.85	0.53	0.22	0.29	5.72	41.24	0.50	0.20	0.27	4.27	63.12	0.64	0.41	0.51	4.35	70.06	0.63	0.38	0.58
FoundIR [34]	5.56	41.41	0.53	0.21	0.28	8.28	29.52	0.50	0.24	0.22	5.15	56.67	0.65	0.44	0.44	5.72	65.41	0.66	0.38	0.51
DFPIR [78]	5.45	48.50	0.58	0.24	0.33	8.33	28.57	0.52	0.19	0.22	4.33	64.22	0.64	0.39	0.52	4.55	69.37	0.62	0.36	0.57
MoCE-IR [109]	5.23	44.07	0.53	0.23	0.30	5.99	43.54	0.51	0.23	0.29	4.27	64.95	0.65	0.43	0.52	4.47	71.48	0.64	0.42	0.60
Ours	4.92	52.27	0.61	0.24	0.39	6.71	32.25	0.57	0.22	0.26	4.74	65.31	0.66	0.40	0.49	4.92	69.84	0.64	0.39	0.59
Method	RealSRR 2×					DrealSRR 2×					RealSRR 4×					DrealSRR 4×				
	NIQE↓	MUSIQ↑	MANIQA↑	CLIPQA↑	TOPIQ↑	NIQE↓	MUSIQ↑	MANIQA↑	CLIPQA↑	TOPIQ↑	NIQE↓	MUSIQ↑	MANIQA↑	CLIPQA↑	TOPIQ↑	NIQE↓	MUSIQ↑	MANIQA↑	CLIPQA↑	TOPIQ↑
<i>State-of-the-art SR methods</i>																				
StableSR [83]	6.62	63.20	0.63	0.63	0.51	6.58	60.31	0.60	0.63	0.51	5.86	58.56	0.57	0.58	0.47	6.91	51.74	0.52	0.58	0.45
DiffBIR [41]	5.97	69.44	0.66	0.70	0.68	5.81	55.69	0.63	0.70	0.67	5.60	69.55	0.65	0.71	0.68	7.00	65.88	0.61	0.71	0.66
SeeSR [98]	5.71	71.46	0.67	0.72	0.72	6.05	67.93	0.65	0.70	0.70	5.47	70.43	0.65	0.70	0.71	6.36	64.96	0.60	0.69	0.67
PASD [103]	5.12	67.67	0.63	0.62	0.61	5.66	55.53	0.61	0.65	0.63	5.21	64.63	0.58	0.58	0.58	6.94	57.85	0.52	0.57	0.55
OSEDif [97]	5.81	70.55	0.66	0.69	0.64	6.02	67.61	0.63	0.69	0.63	5.74	69.14	0.63	0.67	0.63	6.78	62.68	0.58	0.69	0.59
PURE [92]	5.34	69.47	0.66	0.72	0.65	6.18	65.95	0.62	0.70	0.63	5.77	66.84	0.62	0.69	0.61	7.11	60.14	0.57	0.67	0.58
Ours	7.05	51.94	0.53	0.35	0.37	7.67	47.74	0.50	0.34	0.37	7.63	52.65	0.48	0.39	0.40	8.79	46.53	0.44	0.45	0.41

These visualizations cover a broader range of degradations and benchmarks, further illustrating the effectiveness and generalization ability of our FAPE-IR. For clarity, we group the results into two parts: (1) supplementary qualitative comparisons, and (2) visualizations derived from our flow-matching training process.

10.1. More Qualitative Comparisons

Figures 10–11 present additional qualitative comparisons on deraining, desnowing, deblurring, dehazing, denoising, low-light enhancement, and real-world super-resolution. Figure 10 compares FAPE-IR with recent unified models, while Figure 11 focuses on strong AIO-IR baselines. Across all tasks, FAPE-IR introduces fewer artifacts, better respects the input content, and more faithfully preserves high-frequency details than both categories of baselines.

- **Rainy scenes (deraining):** Unified models often hallucinate textures or alter scene layouts, and AIO-IR methods tend to leave residual streaks or over-smooth details. In contrast, FAPE-IR suppresses rain streaks more thoroughly while retaining local texture contrast, consistent

with the improvements in LPIPS and DISTs.

- **Snow scenes (desnowing):** Competing methods either fail to fully remove veiling snow or over-smooth the background. FAPE-IR removes both small particles and large translucent flakes while maintaining the underlying structures of objects such as buildings and vegetation.
- **Denoising:** Under heavy Gaussian noise, unified models may introduce unnatural textures, whereas AIO-IR baselines can blur fine patterns. FAPE-IR better preserves sharp edges and regular patterns (e.g., window grids) with fewer color shifts and blotchy artifacts.
- **Real-world blur (deblurring):** The proposed planner more effectively separates structural edges from noise-like blur, leading to sharper reconstructions with substantially fewer ringing and overshoot artifacts than both unified models and AIO-IR methods.
- **Dehazing and low-light images:** For hazy and under-exposed scenes, baseline methods often exhibit residual haze, elevated noise, or strong color bias. FAPE-IR produces smoother illumination transitions, more balanced global contrast, and more natural color tones.

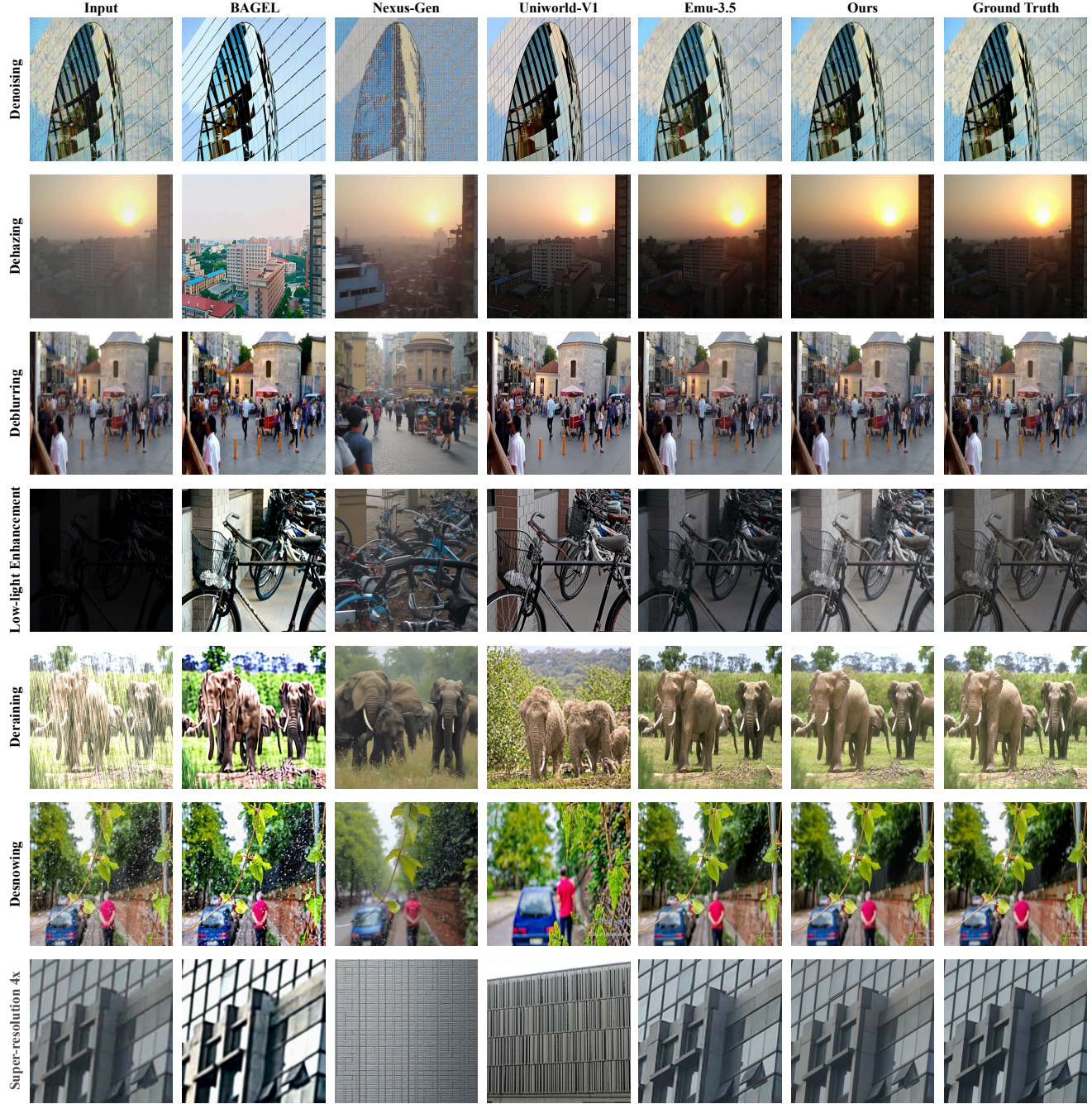


Figure 10. Comparison among unified models, including BAGEL [17], Nexus-Gen [11], Uniworld-V1 [40], and Emu3.5 [16].

- **Super-resolution:** On real-world $\times 4$ super-resolution, unified models sometimes hallucinate high-frequency patterns that deviate from the ground truth, while AIO-IR methods tend to over-smooth repetitive structures. FAPE-IR reconstructs sharper, more regular textures (e.g., building facades) that better match the ground-truth distribution, despite the NR-IQA metrics being challenging and sometimes misaligned with human perception.

These additional qualitative comparisons further corroborate the distortion–perception trade-offs discussed in the main paper and illustrate that FAPE-IR scales more reliably than both unified models and existing AIO-IR approaches across diverse degradation types.

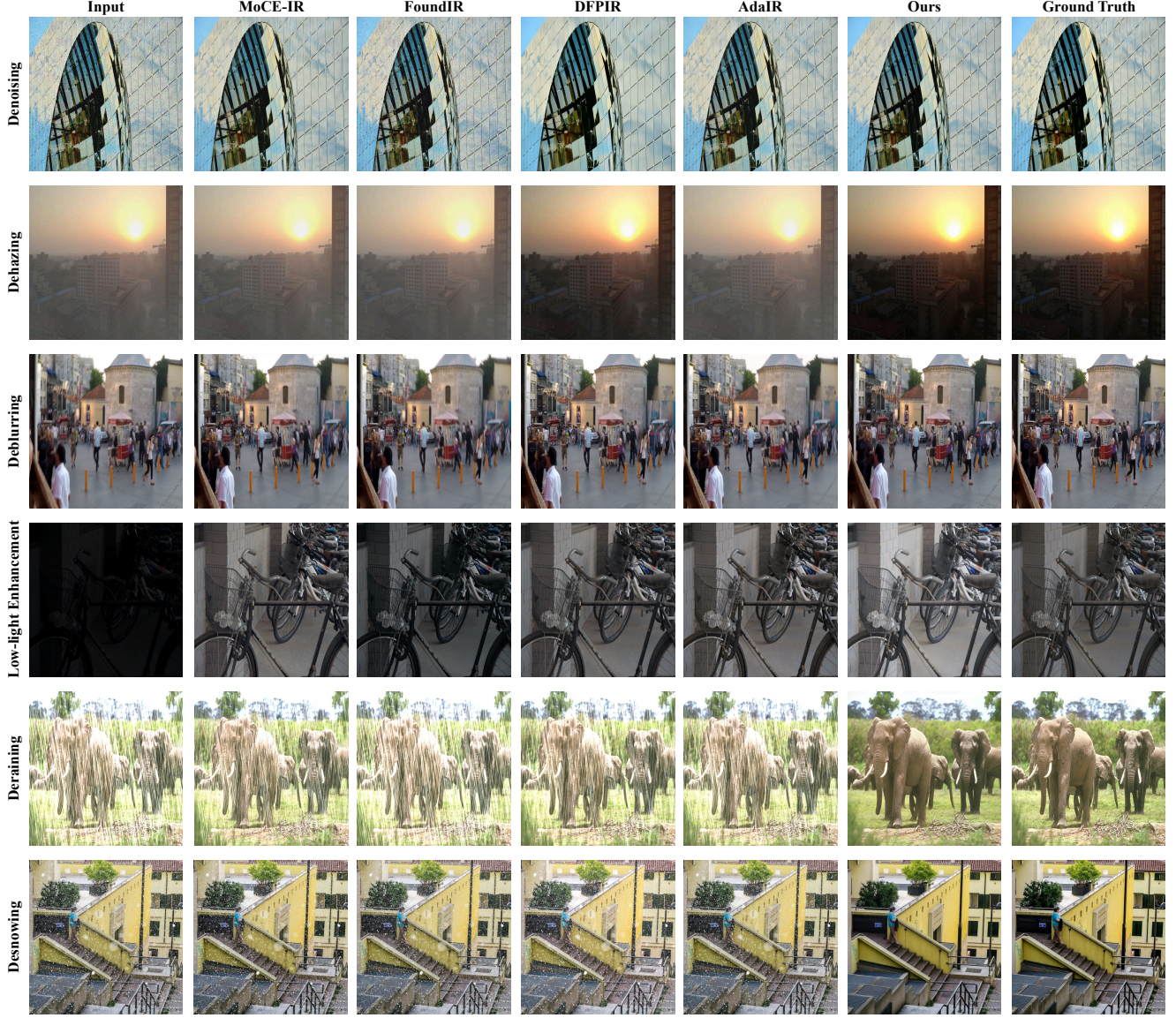


Figure 11. Qualitative comparison of restoration results produced by FAPE-IR and state-of-the-art AIO-IR models.

10.2. Flow-Matching Visualizations

In our early exploratory stage, we attempted to train the entire FAPE-IR framework using a standard flow-matching (FM) objective [45]. Figure 12 shows representative qualitative results on real-world super-resolution benchmarks. While the FM-trained variant is able to remove part of the degradation and produce sharper outputs than the input LR images, it also generates a large number of artifacts and unrealistic details: building facades exhibit irregular, “painted” textures, edges become locally distorted, and fine patterns are often hallucinated rather than faithfully reconstructed from the input. These failure cases provide an empirical counterexample to the naive expectation that FM alone is sufficient for all-in-one restoration in pixel space.

In ill-posed tasks such as real-world SR, the learned flow tends to overfit the training distribution and prioritize distribution matching over content preservation, leading to spurious high-frequency components that hurt perceptual realism. This observation is consistent with our theoretical motivation, and it prompted us to explore additional adversarial training and frequency-aware regularization to better constrain the planner–executor pipeline.

Although this FM-based variant is discarded in our final system, we include it here for completeness, given the widespread use of flow-matching in recent unified generative models. In future work, we plan to investigate ways to mitigate these artifacts, e.g., by incorporating stronger structural priors or geometry-aware constraints into the flow



Figure 12. Qualitative results of training our framework with a standard flow-matching (FM) objective on real-world super-resolution. Although the FM-trained variant can sharpen some structures, it also introduces severe artifacts and unrealistic high-frequency details (e.g., distorted edges and hallucinated textures), which motivates our final design choices for FAPE-IR.

field, so that FM can be more safely integrated into general-purpose restoration frameworks like FAPE-IR.